# EFFECT OF TUNNEL EXCAVATION ON TRANSMISSIVITY DISTRIBUTIONS AND FLOW IN A FRACTURE ZONE

D.D. Tannant*, P.K. Kaiser*, and Chan†, D.H.

* Geomechanics Research Centre, Laurentian University, Sudbury, Ont., Canada P3E 2C6

† Department of Civil Engineering, University of Alberta, Edmonton, Alta., Canada T6G 2C6

Submitted to the Canadian Geotechnical Journal

Dec. 12, 1991

# EFFECT OF TUNNEL EXCAVATION ON TRANSMISSIVITY DISTRIBUTIONS AND FLOW IN A FRACTURE ZONE

D.D. Tannant*, P.K. Kaiser*, and Chan†, D.H.

* Geomechanics Research Centre, Laurentian University, Sudbury, Ont., Canada P3E 2C6

† Department of Civil Engineering, University of Alberta, Edmonton, Alta., Canada T6G 2C6

## Abstract

During an excavation response experiment performed at the Underground Research Laboratory (Atomic Energy of Canada Limited, Pinawa, Manitoba) a decrease in fracture zone transmissivity was measured as a tunnel intersected the Room 209 fracture zone. The decrease in transmissivity was greatest as the pilot and the slash faces passed the fracture zone. The transmissivities increased towards their pre-excavation values as the faces proceeded past the fracture zone. This response suggested that shear stresses or displacements controlled the hydraulic behaviour of the fractures.

The hydraulic response in the fracture zone was analyzed using finite element models. Predictions of shear displacement distributions in the fracture zone as a function of face position were obtained from a three-dimensional finite element model using joint elements to represent the fracture zone. A phenomenological relationship between shear displacement and transmissivity change was used to modify the transmissivity distributions in the fracture zone based on shear displacements for different excavation stages. Seepage analyses with these transmissivities provided predictions that matched closely the field measurements obtained from the Room 209 fracture zone. These results and the inability of conventional, normal stress dependent, fracture closure to predict consistently the hydraulic response support the concept of shear causing a reduction in fracture zone transmissivity. Excavation-dependent, shear-induced reduction in transmissivity provides an alternate mechanism for interpreting and understanding the hydraulic response of disturbed fracture zones.

# 1 Introduction

An excavation response experiment performed at Room 209 of Atomic Energy of Canada Limited's (AECL) Underground Research Laboratory (URL) showed an unexpected decrease in fracture zone transmissivity as a tunnel intersected the Room 209 fracture zone (Lang et al., 1987). When excavations disturb the flow in fracture zones, increases or decreases in transmissivity (hydraulic conductivity times aperture) can occur. Traditionally, fracture zone transmissivity changes are attributed to changes in normal stress on the fractures and transmissivity increases are attributed to shear related dilation. Numerical modelling by Kaiser et al. (1987, 1989) showed that the measured decreases in transmissivity could not be consistently explained by changes in normal stress. Shear-induced decreases in the fracture zone transmissivity are postulated to explain the observed hydraulic response in Room 209.

A shear-dependent fracture zone transmissivity model was developed by Tannant (1990) and introduced in a companion paper by Tannant and Kaiser (1992). This model is based on the observation that shear displacements can reduce the transmissivity of fracture zones by reducing the apertures of flow channels within a fracture zone. The geometric arrangement of fractures in a fracture zone generates a complex pattern of flow channels. For example, in fracture zones with an en echelon arrangement of fractures, imposed shear displacements will reduce the aperture of critically oriented fractures (Fig. 1). This leads to a decrease in the overall fracture zone transmissivity. The shear-dependent fracture zone transmissivity model (Tannant and Kaiser, 1992) provides a simple relationship between shear displacement and transmissivity change in a fracture zone. This approximation of reality is used to relate shear displacements predicted from a finite element model with transmissivity changes in a fracture zone.

>>> Figure 1 Shear-induced reduction in fracture aperture and fracture zone transmissivity.

The concept of an excavation-dependent, shear-induced reduction in transmissivity is validated by use of field data and numerical models. Shear-induced transmissivity reduction contrasts the conventionally held notion of shear displacements causing fracture dilation and hence, a transmissivity increase. Shear-induced transmissivity reduction provides an alternate mechanism for interpreting and understanding the hydraulic response of disturbed fracture zones. This paper, by concentrating on the influence of shear displacements, does not imply that normal stress effects and coupled processes are irrelevant. Instead, we show that shear displacements may dominate the hydraulic response in certain fracture zones.

The shear displacements in the Room 209 fracture zone were generated with a three-dimensional finite element model that approximated the tunnel and fracture zone. A shear-dependent fracture zone transmissivity model introduced earlier (Tannant and Kaiser, 1992) was used to convert shear displacements from the geomechanical model to transmissivity distributions for the seepage model. The seepage model was first calibrated with measured hydraulic parameters in the Room 209 fracture zone. Seepage modelling was then performed with a two-dimensional finite element model representing the planar fracture zone. All modelling was performed assuming elastic fracture zone behaviour and no coupling between fracture zone pressures and rock stresses.

## 2 Room 209 Excavation Response Experiment

### 2.1 Background

The Room 209 excavation response experiment was performed at the Underground Research Laboratory located 100 km northeast of Winnipeg, Manitoba, in the Lac du Bonnet Batholith (Lang, 1989). The excavation response experiment was initiated after exploratory drilling at the 240-m level (Fig. 2) discovered a near-vertical, water-bearing fracture zone (the Room 209 fracture zone) in an otherwise, essentially unfractured rock

mass. This discovery lead to the design and implementation of the Room 209 excavation response experiment. The experiment was conducted to evaluate the response of the rockmass and the fracture zone to the excavation of a tunnel, to assess the effects of the excavation procedure, to refine field monitoring instrumentation, and to test the predictive capabilities of numerical modelling codes. The rockmass around the Room 209 tunnel was monitored with a variety of instruments to achieve these goals. Thompson and Lang (1987), Lang et al. (1987), and Thompson et al. (1989) describe the design of the experiment, the type of monitoring tools, and the instrumentation layout. A summary of the Room 209 excavation response experiment is given by Lang (1989) and a more detailed description of the experiment may be found in Lang et al. (1987).

>>> Figure 2 Cross-section through the Lac du Bonnet Batholith (after Martin et al., 1990a).

## 2.2 Hydro-Geologic Setting

At the URL shaft, a moderately fractured, pink granite grades downwards into a grey granite or quartz monzonite at about 220 m depth (Fig. 2). There are two extensive, shallow-dipping, major fracture zones in the upper 400 m of the batholith at the URL site (Everitt, 1986). These fracture zones define the main aquifers at the site and control the movement of groundwater within the rock mass. Except for these distinct fracture zones, the rock is relatively unfractured.

The predominant lithology of the immediate Room 209 area consists of a grey, unaltered, gneissic, medium grained granite. Room 209 and the entire 240-m level is situated within a wedge shaped block delineated by Fracture Zone #2 below and a splay, Fracture Zone #2.5 above.

The Room 209 fracture zone (Fig. 3) was located 4 m ahead of the development room face. The zone is nearly planar with an orientation of (134°) 79°{dip direction) dip} and is apparently unrelated to the regional, shallow dipping, major fracture zones. This fracture zone is almost perpendicular to the centerline of Room 209, which has a trend of 120°. It is

a composite feature consisting up to six, discontinuous fractures within 0.4 m wide zone near Room 209. It cuts through several granodiorite dykes (Fig. 4) and infillings are absent or very minor. It was not possible to determine, in detail, the internal structure of the fracture zone from drill cores or traces of fractures around the tunnel perimeter. However, it is evident that the fracture zone consists of en echelon fractures.

>>> Figure 3 Plan and section of Room 209 showing fracture zone and packer locations.

Figure 4 shows the extent of the fracture zone as interpreted by Lang et al. (1987). On the northeast side of Room 209, the fracture zone thickens to about 1.5 m at a distance of 15 to 25 m from the tunnel whereas to the southwest, the fracture zones pinches out at roughly 15 m from Room 209.

The Room 209 fracture zone is hydraulically connected to the Fracture Zone #2.5 splay, situated 29 m above the excavation elevation. The fracture zone terminates immediately below the tunnel floor. Based on hydraulic monitoring, this zone appears more permeable above and northeast of Room 209 (Kozak and Davison, 1986).

>>> Figure 4 Extent of Room 209 fracture zone.

### 2.3 Instrumentation

Packers were used to monitor the fluid pressures at different locations around the tunnel and these were installed in two stages. The first set of boreholes (N1, N2, S1, S2, and OC1) was drilled before the development room extension was excavated (Fig. 3b). Packers were placed in these holes to isolate and monitor the hydraulic behaviour in the Room 209 fracture zone using vibrating wire pressure transducers. The 7.5 m long extension to the development room was carefully excavated by drilling and blasting a pilot and slash. Additional monitoring holes (R1, R2, F1, and F2) were drilled from the end of the development room. As before, packers and pressure transducers were installed to monitor the hydraulic pressures. The packer systems used by AECL are described by

Thompson et al. (1989). Eight of these boreholes, all within 2.5 m of the tunnel periphery were situated to measure the near-field hydraulic response. OC1 was drilled to intersect the fracture zone at about 15 m to the northeast of the tunnel axis. This borehole was placed to provide a measurement point outside the tunnel's zone of influence on rock stresses.

## 2.4 Measured Hydraulic Response to Tunnel Excavation

Several hydraulic tests were performed before the tunnel was advanced including fluid withdrawal tests in boreholes OC1, N1, N2, R1, R2, and F1. By testing one borehole at a time the relative transmissivity distribution or connectivity between the boreholes was established. Figure 5 summarizes the findings of these tests (Kozak and Davison, 1986). The band of low transmissivity cutting through Room 209 from the upper northeast side to the lower southwest side appears related to the presence of a cross-cutting granodiorite dyke (Fig. 4).

>>> Figure 5 Hydraulic interconnection from borehole interference testing (after Kozak and Davison, 1986).

After initial fracture zone characterization, Room 209 was excavated by the drill and blast technique (Kuzyk et al., 1986; Lang et al., 1987). A pilot tunnel was advanced a distance of 25 m in ten rounds. The time between blast rounds ranged from 57 to 73 hours allowing sufficient time to reach steady-state flow conditions in the fracture zone (Lang et al., 1987). The slashing excavation proceeded after the pilot tunnel was completed (Fig. 3b).

Fluid pressures were continuously monitored during the excavation of Room 209. In addition, fluid withdrawal tests were performed between blast rounds. All measurements are reported by Lang et al. (1987). The measurements related to the fracture zone response include: 1) steady-state fluid pressures as a function of time (or excavation stage); 2) the flow gradient ($Q/\Delta H$) obtained from single or multi-step fluid withdrawal tests; 3) the rate of flow from blast-holes that intersected the fracture zone prior to blasting through the

fracture zone; and 4) the rate of flow into the pilot and the slash after excavation through the fracture zone.

Figure 6 presents measurements of flow gradient relative to the excavation face position. The ratio of flow to head change or flow gradient provides a measure of fracture transmissivity or equivalent hydraulic fracture aperture (using for example, the parallel plate flow model). The flow gradient at the packed-off intervals, first dropped as the excavation face passed the fracture zone, then partially or fully recovered as the excavation advanced. These characteristic drops and recoveries in the flow gradient are similar to the variation in shear stress as an excavation face passes a measurement location.

>>> Figure 6 Measured flow gradients at the Room 209 packer locations (Data from Lang et al., 1987).

Three packers (F1, F2, and S1) failed to function after the pilot intersected the fracture zone. The data from the S2 packer after the pilot had intersected the fracture zone is of questionable accuracy because of poor packer performance. All other packers performed well throughout the excavation response experiment and provided reliable data for comparison with predictions.

The approach adopted to examine the hydraulic response was divided into four phases: 1) finite element calculation of shear displacement distributions in the fracture zone at different excavation stages, 2) determination of an initial, best-fit pre-excavation transmissivity distribution for the fracture zone, 3) estimation of the transmissivity distributions using the calculated shear displacements, and 4) comparison of the predicted and measured hydraulic responses at different excavation stages.

## 3 Geomechanical Finite Element Model of Room 209

A major step in the process of evaluating the hypothesis of a shear-dependent, fracture zone transmissivity reduction and interpreting the partial recovery is the prediction of shear displacements in the Room 209 fracture zone. Due to the complex geometry and

in situ stresses that characterize the Room 209 experiment, a three-dimensional finite element model was used to generate the shear displacements.

### 3.1 Finite Element Mesh and Coordinate System

The three-dimensional mesh constructed to represent the area around the Room 209 fracture zone contains 3680 isoparametric elements with 8161 nodes (Fig. 7). The central portion of the mesh is shown in Figure 7b. The geometry of the pilot and slash cross-sections approximates the as-excavated geometry near the Room 209 fracture zone. In the longitudinal direction (z-axis), the mesh consists of 20 slices of elements including one slice of joint elements representing the fracture zone (Fig. 8). Quadratic elements were used for elements near the tunnel and fracture zone while linear (8-noded) elements were used elsewhere.

>>> Figure 7 Three-dimensional finite element mesh and cross-section of the inner part of the mesh.

>>> Figure 8 Longitudinal section through one half of the finite element mesh showing joint elements and slice orientations.

The displacement boundary conditions imposed on the mesh were rollers at each end of the mesh, i.e., on the two planes perpendicular to the tunnel axis, whereas the remaining nodes on the outer surface of the mesh were fixed. The radial distance to the outer boundary was about 37 m and the length of the mesh was 60 m (Fig. 7).

The finite element analyses were performed using the code SAGE (Chan, 1986) on the Cyber 205 computer located at the University of Calgary.

### 3.2 In Situ State of Stress

The following stress tensor was assumed to best represent the in situ stress state near Room 209 (Martin et al., 1990b; Martin, per. comm., 1990):

Table 1 In situ stresses

| Principal Stress | Magnitude (MPa) | Plunge (deg) | Trend (deg) |
|---|---|---|---|
| $\sigma_1$ | 27.5 | 25 | 213 |
| $\sigma_2$ | 14.4 | 48 | 092 |
| $\sigma_3$ | 9.8 | 31 | 320 |

This stress field corresponds to a normal stress of 10.5 MPa and a maximum shear stress of 2.1 MPa in the plane of the fracture zone.

### 3.3 Material Properties

The material properties of the solid elements were chosen to represent rock that is homogeneous, isotropic and linear elastic. The rock mass around the Room 209 fracture zone has been extensively tested for physical properties (Lang et al. 1986; Lang 1989; Katsube and Hume, 1987; Koopmans and Hughes, 1988; 1989a,b). The measured rock mass modulus $E$ is slightly anisotropic and heterogeneous. Although some modulus anisotropy occurs near Room 209, there was insufficient information to assign spatial variations in modulus to the finite elements. Therefore, a homogeneous, isotropic rock mass modulus was adopted for the numerical model. Based on the modulus data and previously reported back-analyses, an isotropic rock mass modulus of 60 GPa and a Poisson ratio of 0.25 were selected.

In situ testing after the excavation of the tunnel (Koopmans and Hughes, 1989a,b) indicated lower moduli near the tunnel walls. This modulus reduction is probably caused by blast damage and confining stress dependent softening. Thus, the modulus of elements located in the first ring, immediately adjacent to the tunnel walls was reduced to 40 GPa and the second ring of elements was assigned an intermediate modulus of 50 GPa (Fig. 9). The modulus of elements directly ahead of the tunnel face was also reduced to 50 GPa.

the laboratory testing environment, sample disturbance. Relationships between shear stress and shear displacements induced under nearly constant normal stresses similar to those experienced by the Room 209 fracture zone (10 to 11 MPa) gave a wide range of shear stiffnesses, typically less than 1 to more than 1000 MPa/mm. These stiffnesses are for single fractures and it is not known how they would relate to a system of fractures with a complex geometry composing the fracture zone at Room 209. Other laboratory work (Goodman and Dubois, 1972; Sun et al., 1985; Chappell, 1990) has shown that the shear stiffness of fractures is less than the normal stiffness at a given normal stress. The ratio between shear and normal stiffness for single fractures in crystalline rock ranged between 4.2 (Goodman and Dubois, 1972) and 20 to 50 (Sun et al., 1985). Also, it is possible that a fracture zone is softer in shear than a single fracture. The empirical shear stiffness relationship by Barton and Bakhtar (1983) predicted a stiffness of about 2 MPa/mm. For the numerical model, a fracture zone stiffness of 3 MPa/mm was finally selected. This is the same value used by Kaiser et al. (1989) and equals the value used by Rutqvist et al. (1990) for crystalline rock fractures subject to 10.2 MPa normal stress.

### 3.4 Excavation Sequence

The analysis consisted of three main excavation stages: 1) development room, 2) pilot, and 3) slash. The excavations of the pilot and the slash were further subdivided into numerous steps. These excavation steps correspond roughly with the blast rounds on either side of the fracture zone. In addition, both the pilot and the slash were excavated to the fracture zone. The excavation sequence is summarized in Table 2.

Table 2 Excavation sequence

| Excavation Step | Designation | Face Distance from Fracture Zone (m) |
|---|---|---|
| Development Room | DR | - 4 |
| Pilot | P1 | -1.2 |
| Pilot (FZ) | P2 | 0 |
| Pilot | P3 | 1.2 |
| Full Pilot | P4 | 28 |
| Slash | S1 | -2.0 |
| Slash (FZ) | S2 | 0 |
| Slash | S3 | 0.5 |
| Full Slash | S4 | 28 |

The pilot and slash face positions approximate the as-excavated, average face positions. However, the actual excavation of Room 209 did not have excavation rounds corresponding to the modelled steps of P2 and S2. These steps were added to capture the high stress and displacement gradients that exist near the tunnel face.

### 3.5 Shear Displacements in the Fracture Zone

At Room 209, most field monitoring, including the hydraulic testing, was conducted after the development room had been excavated. Test data obtained after excavation of the development room and before the pilot excavation were used to establish the initial fracture zone conditions. Therefore, the fracture zone displacements were calculated relative to the conditions after the excavation of the development room. Shear displacements in the fracture zone were determined from the differential nodal displacements on either side of the fracture zone.

Contour plots of the maximum shear displacements after each of the pilot and the slash excavation steps are presented in Figures 10 and 11. These plots clearly show the evolution of shear displacements as the excavation face approaches, intersects, and then

passes the fracture zone. The shear displacements at step P1 (Fig. 10a), are generally less than 0.1 mm and only just beginning to develop. However, a further advance of 1.2 m (P2) intersects the fracture zone and establishes much larger shear displacements (Fig. 10b). The shear displacement distribution is strongly non-axisymmetric because of the in situ stress field, and to some extent, the fracture zone orientation and tunnel geometry. Figures 10a and 10b suggest a plane of "near symmetry" extending from the upper-north to the lower-south of the fracture zone. The orientation of this plane is similar to the orientation (in the plane of the fracture zone) of the major principal stress. After the pilot proceeded beyond the fracture zone, the shear displacements rapidly decrease (Fig. 10c) and then approach a stable distribution (Fig. 10d).

>>> Figure 10 Maximum shear displacement magnitudes in the fracture zone during pilot excavations.

>>> Figure 11 Maximum shear displacement magnitudes in the fracture zone during slash excavations.

The shear displacements at S1 (Fig. 11a) are very similar to P4 with a slight increase in magnitude. However, as the slash intersects the fracture zone (Fig. 11b), shear displacements again increase at the roof and south side. The slash at S2 generates approximately half the shear displacements the pilot created at P2 even though the total volume excavated is 1.5 times that of the pilot. Again, as the face passes the fracture zone the shear displacements decrease (Fig. 11c) and approach stable distributions (Fig. 11d).

A comparison of the shear distributions at steps P2 and S2 shows that the high shear displacement lobe on the upper-north side of the tunnel at P2 shifts upwards to the roof. The other lobe of high shear displacement remains in roughly the same position and orientation. This upward shift in one lobe of shear displacements may be a result of slashing only the roof and side-walls.

It is important to note that the final shear displacements after the pilot and the slash excavations are non-zero despite the elastic model used for both the rockmass and the fracture zone. These permanent displacements are caused by the release of initial shear stresses in the fracture zone.

The shear displacement distributions, plotted in Figures 10 and 11, were used to determine shear-dependent transmissivity changes for fracture zone seepage modelling. The seepage analysis required elemental displacements, i.e., one representative shear displacement per element. These displacements were obtained by taking the relative displacement components at nodes belonging to each element and calculating the average shear displacement for each element in the seepage mesh. These shear displacements were then transformed into transmissivity changes for each element using the flow model by Tannant and Kaiser (1992). The seepage modelling and associated calculations of transmissivity distributions are discussed in the next section.

## 4 Room 209 Seepage Modelling

The finite element modelling of the hydraulic response in the Room 209 fracture zone was conducted in two phases. First, a series of finite element seepage analyses were performed to match, in a trial and error fashion, the pre-excavation or undisturbed transmissivity distribution in the Room 209 fracture zone. Second, the shear displacements determined from the geomechanical modelling were used to generate modified transmissivity distributions at different excavation steps. The relationship between shear displacement and transmissivity change presented by Tannant (1990) was adopted to calculate the new transmissivities after each excavation step. Predictions from seepage analyses using these transmissivity distributions were then compared to the field measurements.

### 4.1 Finite Element Mesh and Boundary Conditions

The finite element mesh presented in Figures 12 and 13 was based on the cross-section of the mesh used for modelling the geomechanical response of Room 209 (Fig. 7). The mesh consisted of 193 four-noded quadrilateral elements containing 205 nodes. Each element was associated with a unique transmissivity set. Therefore, different transmissivity distributions were created by altering 193 different transmissivity values.

>>> Figure 12 Two-dimensional finite element mesh for seepage analyses.

>>> Figure 13 Inner part of finite element seepage mesh (Fig. 12) showing pilot and slash and nodes representing packer locations.

The boundary conditions for the mesh shown in Figure 12 are: 1) no-flow at the right and lower peripheries of the mesh representing the disappearance or pinching out of the fracture zone; 2) a prescribed head at the upper and left boundaries of the mesh reflecting the contact with a major fracture zone above Room 209 and a zone of greater fracture zone storativity and permeability about 100 m to the northeast of Room 209. The prescribed head of 74.6 m along the upper mesh boundary corresponds to the steady-state pre-excavation head (108.6 m or 1065 kPa fluid pressure) measured at the elevation of Room 209 (Lang et al., 1986; 1987). The heads along the left mesh boundary were specified to increase hydrostatically with depth from a head of 74.6 m at the upper northeast corner (point A) to 139.3 m at the lower northeast corner (point D). These boundary conditions are based on the hydro-geologic features near the Room 209 fracture zone as depicted in Figure 4.

### 4.2 Pre-Excavation Transmissivity Distribution

The transmissivity distribution in the fracture zone prior to excavation of the pilot was obtained by altering transmissivities of individual elements and performing seepage analyses to compare predicted with measured hydraulic responses. The best fit was established by minimizing the difference between measurements and predictions of the flow

gradient and heads at the packer locations as well as flows from the blast holes. Isotropic flow was assumed within each element. The quality of fit between the mesh transmissivities and actual fracture zone transmissivities is influenced by the size of elements in the mesh, the available field data, and the variability and reliability in the measured values.

The best-fit transmissivity distribution (with transmissivities converted to equivalent parallel-plate apertures for presentation) is shown in Figure 14. Only the near-field elemental apertures are shown in this figure. The transmissivity distribution accounts for the hydro-geologic features noted near Room 209 (Figs. 4 and 5). For example, the band of low transmissivity elements extending from the lower right to the upper left of the tunnel corresponds to the presence of a granodiorite dyke. The lower transmissivity of the dyke is inferred from borehole pressure interference tests conducted before the pilot excavation (Kozak and Davison, 1986). The low transmissivities in the lower right part of the mesh conform to a disappearance of the fracture zone at this location.

>>> Figure 14 Initial best-fit transmissivity (aperture) distribution in the Room 209 fracture zone.

Figure 15 compares the predicted steady-state heads and flow gradients with measured values. The range in measured values is indicated by two extremes, the measured low and the measured high values. Figure 15a shows that the predicted steady-state heads are very close to those measured confirming that the selected boundary conditions portray field conditions well.

Fluid withdrawal tests were conducted at the nodes representing the packers (Fig. 13). A packer test was simulated by specifying a negative flow at a node and allowing the program to determine the corresponding head. The head drop resulting from the prescribed flow could then be calculated. The head changes at other nodes during the packer tests were used for cross-hole interference analyses. Results from simulated fluid

withdrawal tests presented in Figure 15b show that the transmissivity distribution near the packer locations is comparable to that expected in the field with all predictions falling within the range of measured values.

>>> Figure 15 Comparison between measured and predicted heads and flow gradients from the Room 209 fracture zone.

The predicted response of the seepage model and the correspondence between the transmissivity distribution and the hydrogeologic features in the Room 209 fracture zone provide evidence that the initial transmissivity distribution presented in Figure 14 is a good representation of the near-field transmissivity distribution of the Room 209 fracture zone.

### 4.3 Transmissivity Distributions Based on Shear Displacements

The evaluation of excavation or shear-dependent transmissivities involved calculation of transmissivity distributions corresponding to each excavation stage modelled earlier to determined shear displacements. All changes in fracture zone transmissivity resulting from excavation-induced shear displacements are taken relative to the initial distribution (Fig. 14). The changes in transmissivity for each excavation step were calculated from the shear displacements using Equation 10 given by Tannant and Kaiser (1992):

For the flow model presented in Figure 1, the aperture changes are only a function the shear displacement and the angles between the direction of shearing and the orientation of the primary ($\alpha$) and secondary fractures ($\psi$).

[1] $$a_{p2} = a_{p1} + \delta \sin \alpha \quad \text{and} \quad a_{s2} = a_{s1} - \delta \sin(\psi - \alpha)$$

where the subscript '1' refers to the initial aperture and '2' refers to the aperture after shear displacement ($\delta$). The transmissivity of the fracture zone ($T_{fz}$) after shear displacement can be determined if the initial geometry and the magnitude and direction of shear displacements are known:

[2] $$T_{f2} = c\left[\frac{l_p \cos\alpha + l_s \cos(\psi - \alpha)}{\frac{l_p}{a_{p2}^3} + \frac{l_s}{a_{s2}^3}}\right]$$

where the apertures $a_{p2}$ and $a_{s2}$ are given by Equation 1 and $l_p$ and $l_s$ are the lengths of the primary and secondary fractures. When a primary or secondary fracture closes, the fracture zone transmissivity drops gradually to zero. In reality, a minimum or irreducible transmissivity exists below which shear causes no further transmissivity decrease. This minimum transmissivity was arbitrarily chosen at $7.8 \times 10^{-11}$ $m^2/s$ (or an equivalent aperture of 5 μm) for the modelling of the Room 209 fracture zone.

The geometric structure of the fractures in the Room 209 fracture zone could not be determined. Therefore, the least complex form of the shear-transmissivity relationship was adopted. Equation 2 was used under the following assumptions: 1) the primary fractures are inclined 45° to the fracture zone and the secondary fractures are perpendicular to the primary fractures; 2) the initial apertures of the primary and secondary fractures are equal, but vary with location throughout the fracture zone as reflected in the initial transmissivity distribution (Fig. 14); 3) the relationship between shear displacement and transmissivity change is isotropic.

The selected orientations of the primary and secondary fractures create a relationship that is independent of the direction of shear displacement. Note, the fracture zone flow model presented in Figure 1 is a phenomenological model used to derive the shear-transmissivity change relationship. This model does not represent, in a physical sense, the real fracture structure in the Room 209 fracture zone since it does not account for the three-dimensional nature of the flow paths or shear direction-dependent changes in transmissivity.

Initial application of Equation 2 with the shear displacements shown in Figures 10 and 11 yielded excessive transmissivity reductions (the fracture transmissivity dropped to zero almost everywhere around the opening). Because the choice of shear stiffness for the

joint elements was somewhat subjective, the shear displacements were reduced by a factor of five prior to use in the shear-transmissivity change relationship. This resulted in more realistic transmissivity distributions. Alternatively, the form of the shear displacement - transmissivity change relationship or the assumptions listed above could have been altered such that the shear displacements would cause more realistic transmissivity changes. Reducing the shear displacements should be roughly equivalent to increasing the shear stiffness of the joint elements by a factor of five. An increase in shear stiffness to 15 MPa/mm would make the normal stiffness to shear stiffness ratio equal to 20. This is comparable to the minimum ratios of 10 to 20 suggested by Bandis (1990). These choices were made because of a lack of data and could only be verified by a major project of field investigation.

### 4.3.1 Transmissivity Distributions and Seepage Modelling

The transmissivity distributions near the tunnel for the different excavation steps are depicted by showing the equivalent single fracture apertures in Figures 16 and 17. The high shear displacements associated with step P2 create a continuous ring of low transmissivity (aperture) around the opening. The transmissivity or aperture distributions at the other excavation steps vary as a function of the shear displacements. For example, the increase in shear displacements at the north wall from step P3 to P4 (Figs. 10c and 10d) results in a corresponding decrease in aperture at the wall (Figs. 16c and 16d). It is worthwhile noting that the low transmissivity ring present when the pilot face is at the fracture zone (Fig. 16b) partially opens when the face passes the fracture zone (Figs. 16c and 16d)

>>> Figure 16 Transmissivity (aperture) distributions during pilot excavation based on shear displacements.

>>> Figure 17 Transmissivity (aperture) distributions during slash excavation based on shear displacements.

During the slash excavation, large shear displacements were generated at step S2 (Fig. 11b). The higher shear displacements occurred at the roof and south wall. Hence, a band of low transmissivity extends from the roof to the floor along the south side of the tunnel (Fig. 17b).

The distribution of transmissivity near the opening has a dominant control on the hydraulic response in the fracture zone. The steady-state heads and tunnel inflows were determined by series of finite element seepage analyses using the transmissivity distributions presented in Figures 16 and 17. In addition, fluid withdrawal tests were simulated at each packer location for each transmissivity configuration.

### 4.3.2 Flows into the Tunnel

Figure 18 presents the flows in to the tunnel from the fracture zone. The flows were calculated from the elements around the perimeter of the tunnel. The length of the arrows corresponds to the discharge magnitude while the orientation of the arrows gives the direction of flow. The locations of highest inflow are situated where the ring of low transmissivity has gaps. These regions of higher transmissivity exist at the north wall and roof. No significant flow is predicted through the floor or south wall at any excavation step. At excavation step P1 the fracture zone had not yet been intersected by the pilot. When the pilot excavation intersects the fracture zone at step P2 the high shear displacements generated a complete ring of very low transmissivity around the tunnel. This ring of low transmissivity essentially prevented any inflow. The location and directions of inflow at the other excavation steps are presented in Figure 18.

>>> Figure 18 Specific discharges into Room 209 at different excavation steps and total inflows.

The measured inflow after the pilot was roughly 300 ml/min and after the slash 450 ml/min (Lang et al., 1987). These measurements are only approximate yet they compare favourably with the total inflows predicted from the seepage modelling (Fig. 18). Furthermore, the observed inflows were seen coming from the roof and north side of the tunnel and these locations are predicted by the seepage model.

### 4.3.3 Steady-State Heads

The head distributions or heads at the packer locations are not controlled by the transmissivity magnitudes but by the spatial distribution of the transmissivities around the tunnel. This is in contrast to the flow gradients which are more sensitive to the magnitude of transmissivities in the area near the packer. Figure 19 presents a comparison between measured and predicted heads at all packer locations for all excavation steps. For a perfect fit, all points would lie on the dashed line. Most points fall within a range of $\pm$ 10 % to the dashed line. A difference of less than 10% between measurements and predictions is considered a good fit. The points for S1 (step P2), N2 (steps P3 and S2), and N1 (steps P3 and S2) show larger deviations. However, data from steps P2 and S2 are subject to the greatest uncertainty due to face effects, possible non-linear rock responses, and high stress and displacement gradients. The predicted heads after the pilot (step P4) and the slash (step S4) show excellent correspondence to the measured heads. Measured heads that are higher than those predicted suggest under estimation of the shear - transmissivity dependency.

>>> Figure 19 Measured and predicted steady-state heads at all packers for all excavation steps.

Figure 20 shows the head profiles at the north side (horizontal profile) and above the tunnel (vertical profile) after excavation of the pilot (step P4) and the slash (step S4). This figure clearly shows the improvement in predicted heads when shear-dependent

transmissivity is considered. For comparison, heads predicted without accounting for shear-dependent transmissivity changes (no shear) are also plotted on Figure 20. The head gradient must be extremely high near the tunnel to match the measured heads at 1 to 2 m from the wall. This high pressure gradient is strong evidence for a band of low transmissivity existing around the tunnel between the wall and the packer locations.

>>> Figure 20 North and roof predicted head profiles.

These simulations demonstrate that a transmissivity decrease near the tunnel (dependent on excavation advance) is needed for correspondence between measured and predicted heads. The 'no shear' heads are consistently less than the measured and predicted heads at all excavation steps after the pilot intersected the fracture zone. The incorporation of shear-dependent transmissivities causes an increase in steady-state heads. These heads are much closer to the measured heads when compared to the heads obtained from the initial (no shear) transmissivity distribution.

### 4.3.4 Fluid Withdrawal Tests

Fluid withdrawal tests were simulated numerically at the various packer locations. The flow gradients were determined by withdrawing a known quantity of fluid at the node representing the packer location and determining the corresponding drop in head relative to the steady-state head prior to the packer test. As noted earlier, this technique for simulating packer tests is mesh dependent. Although the magnitude of the flow gradient at any node depends on the mesh refinement near that node, the changes in flow gradient (increases or decreases) are valid indications of changing hydraulic conditions in the fracture zone.

Figure 21 compares the measured and predicted flow gradients at all packers as a function of time. The days when the pilot and the slash intersected the fracture zone are also shown. The wide range in flow gradient magnitudes necessitated separation of the figure into two parts. The north, roof, and OC1 packers were situated in a region of relatively high transmissivity and hence, the flow gradients are high (Fig. 21a). The

predictions best match the measured responses at these packers. This is encouraging since these packers also provided the most reliable field measurements and these results are discussed in greater detail later.

>>> Figure 21 Measured and predicted flow gradients versus time or excavation sequence for Room 209.

Because the OC1 packer was beyond the zone influenced by the tunnel excavation there was essentially no change in transmissivity near the packer and hence, both measured and modelled flow gradients are nearly constant during the excavation (Fig. 21a). The floor and south packers were in a region of low transmissivity and near the boundary of the fracture zone. In areas of low transmissivity, slight shear displacement can easily disrupt the flow. Hence, the transmissivity and flow gradient are extremely sensitive to any disturbance. The floor and S1 packers failed to function after the pilot had intersected the fracture zone (Fig. 21b). Predicted data for these packers are only shown until the P2 excavation steps. The predicted flow gradients at S2 displays the same trend as those measured except that the predicted values vary over a wider range. Considering the extremely low flow gradients in the order of $10^{-9}$ $m^2/s$, the correspondence between predictions and measurements is good. Note that both the measured and predicted flow gradients drop as the face passes the fracture zone and then the recovery as the excavation proceeds.

The predicted flow gradients drop essentially to zero for all packers when the excavation face intersects the fracture zone (Fig. 21b). The measured values did not drop below $1 \times 10^{-9}$ $m^2/s$ suggesting that perhaps the minimum or irreducible transmissivity is higher than the assumed value of $7.8 \times 10^{-11}$ $m^2/s$. A minimum transmissivity seems reasonable since experimental evidence has shown that even when fractures are subject to extremely high normal stresses there is usually a component of irreducible flow (Raven and

Gale, 1985; Pyrak-Nolte et al., 1987). Similarly, under shear it is unlikely that a fracture can be completely closed off; there will always be a small, residual amount of flow.

Figure 22 shows only the data from the north and roof packers. Fluid withdrawal tests at the north and roof packers provided the best field data for comparison with modelling results. The predicted flow gradients obtained using the transmissivity distributions generated by the excavation-induced shear displacements are plotted on Figure 22 with individual, larger square and circular symbols. In addition, Figure 22 shows the influence of the change in hydraulic boundary conditions each time the excavation intersected the fracture zone by solid and dashed lines.

>>> Figure 22 Measured and predicted flow gradients at the north and roof packers compared with predicted flow gradients assuming no transmissivity changes due to excavation.

The change in hydraulic boundary conditions that occurs each time the excavation intersects the fracture zone has a pronounced effect on measurements of flow gradients taken near the excavation. Given a situation in which the transmissivity remains constant, Tannant and Kaiser (1991) have shown that the imposition of a zero pressure boundary condition (a new excavation for example) will increase the measured flow gradients. Figure 22 shows the increase in flow gradients predicted for the north and roof packers when the pilot and the slash intersect the Room 209 fracture zone. These predictions were made by keeping the initial, best-fit transmissivity distribution unchanged during seepage analyses for both excavations. Therefore, had the excavation of Room 209 not altered the transmissivities in the fracture zone, the solid and dashed lines would represent the predictions of the hydraulic response. Furthermore, any meaningful comparisons between predictions and measurements must take into account the effect of changed boundary conditions.

The north and roof packers are close to the tunnel and the flow gradients are influenced by changes in boundary conditions and by changes in transmissivity

distributions. Shear displacements generated near the tunnel cause an associated transmissivity reduction. The resulting zone of reduced transmissivity near the tunnel causes the flow gradients to decrease. Since the shear displacements vary depending on the position of the excavation face, the transmissivity distribution and flow gradients display excavation dependency.

Figure 22 shows that most of the flow gradients measured after the excavation face intersects the fracture zone are smaller than those before intersection. This implies that the transmissivity reduction has a greater influence than the altered boundary conditions. The increase in the predicted flow gradients at the north packers during the slash is caused by the shift in shear displacements to the roof and south sides for step S2 (Fig. 11b). This shift resulted in temporarily higher transmissivities at the north wall of the tunnel for step S2. At the roof, measurements of the flow gradient dropped markedly as the slash intersected the zone and remained roughly constant thereafter. Because the flow gradients do not recover, it is possible that the shear-induced displacements caused non-recoverable damage to the flow paths. The assumption of an elastic (or recoverable) shear-transmissivity relationship may require modification to better predict this response.

## 5 Discussion

The measured and predicted hydraulic responses correspond best for the pilot excavation steps. Predictions of the flow gradients based on shear-dependent reductions in transmissivity are close to those measured and both are significantly lower than results based on a constant transmissivity model. Indeed, without a transmissivity reduction the flow gradients would abruptly increase when the excavation face intersected the fracture zone (due to the boundary condition effect). After the pilot excavation intersects the fracture zone the measured flow gradients recover to nearly their pre-intersection values. This recovery in flow gradients is evidence that the transmissivity distribution is excavation dependent.

The reduction in fracture zone transmissivity is especially apparent in the very high measured and predicted hydraulic heads near the excavation. Hydraulic heads predicted without an excavation-dependent decrease in transmissivity are much lower than those measured. The transmissivity distribution predicted around the perimeter of the tunnel generated localized inflows that occurred at the same locations as were observed in the field. Furthermore, the quantity of inflows predicted by the seepage modelling was close to that measured in the Room 209 tunnel.

All predicted hydraulic parameters: heads, hydraulic gradients, flows, flow gradients, and locations of inflow correspond well with measurements and field observations. Excavation steps that showed greater discrepancy between measurements and predictions (such as at the roof packers for steps S3 and S4) suggest that the simple modelling approach adopted here requires additional improvements. Therefore, further research is needed to refine the relationship between shear displacements and transmissivity changes. However, despite some uncertainties in parameters and the simple phenomenological nature of the flow model, the consistency between field data and predictions provides evidence supporting the concept of excavation-dependent, shear-induced reduction in fracture zone transmissivities.

It is recognized that normal stresses have an influence on fracture transmissivity and certainly normal stresses play some role in the Room 209 fracture zone. For example, an increase in normal stress at the roof may have induced non-recoverable fracture closure that resulted in the flow gradients remaining low after the slash intersected the fracture zone. However, the shear-induced transmissivity reduction mechanism provides a consistent explanation for the observed response at all locations around the tunnel and for all excavation stages. This does not preclude the possibility that normal stress and fracture closure are contributing to the observed hydraulic response, rather it suggests that shear displacements dominate the hydraulic response.

Other possible mechanisms that can influence the hydraulic response in fracture zones include turbulent flow and fracture blockage by rock particles from blasting or sheared asperities. However, these alternatives do not provide a mechanism consistent with the excavation-dependent recovery in the flow gradients. Furthermore, whereas turbulent flow may increase the hydraulic gradient near an opening, it is not possible for it to generate the extremely high hydraulic gradients that exist near the wall of the Room 209 tunnel. In addition, these high pressure gradients (approximately 1 MPa/m) would likely remove any crushed rock particles generated during the excavation process. The changes in the normal stress acting on the fracture zone (Kaiser et al., 1989) could not consistently explain all the observed changes in transmissivity around the tunnel. Only shear displacements that cut off flow channels in the fracture zone seem to provide the necessary mechanism for generating the high pressure gradients.

## 6 Conclusion

When the Room 209 fracture zone was penetrated by a tunnel, a partially recoverable, excavation-dependent reduction in transmissivity was measured. The decrease in transmissivity was greatest as the tunnel face (both for the pilot and the slash excavation) passed the fracture zone. The response of this fracture zone suggested that shear displacements were controlling the hydraulic behaviour. A shear-dependent fracture zone transmissivity model (Tannant and Kaiser, 1992) was used to ascertain whether this mechanism could be responsible for the observed hydraulic response in the fracture zone.

A three-dimensional finite element model with joint elements was used to estimate the shear displacements in the fracture zone. The shear displacements were largest near the perimeter of the tunnel but varied considerably in magnitude at different locations around the tunnel. These shear displacements were used with a phenomenological relationship between shear displacement and transmissivity change to modify the pre-excavation transmissivity distribution in the fracture zone for different excavation stages.

The pre-excavation transmissivity distribution for the seepage model was established based on field characterization of the fracture zone. The transmissivities predicted during the tunnel excavation dropped significantly when the tunnel face intersected the fracture zone and tended to recover somewhat as the excavation proceeded. Seepage analyses with these transmissivities provided predictions that closely matched the field measurements.

The hydraulic response of the fracture zone is controlled by a combination of factors that include: 1) the pre-existing transmissivity distribution, 2) the hydraulic boundary conditions (that change when the tunnel face intersects the fracture zone), and 3) the modifications to the transmissivity distribution in the fracture zone cause by excavation induced shear displacements. The shear displacements play an important role in causing a partially recoverable decrease in transmissivity as the tunnel intersects the fracture zone. The shear displacements resulted in transmissivity distributions that gave very high heads and hydraulic gradients near the tunnel. In addition, the distribution of transmissivities resulted in highly localized flow into the tunnel. The decrease and recovery in both predicted and measured flow gradients as a function of the tunnel face position demonstrates the excavation-dependent nature of the transmissivity distributions arising from the induced shear displacements.

The use of field data and numerical models has demonstrated that the concept of an excavation-dependent, shear-induced reduction in transmissivity is a potential mechanism to explain the observed hydraulic response in the Room 209 fracture zone. Coupled with the inability of conventional, normal stress dependent fracture closure to predict the hydraulic response, the evidence for this concept is compelling.

## Acknowledgments

This research was conducted with some financial support from Atomic Energy of Canada Limited and enthusiastic support by Mr. Peter Lang and Mr. Derek Martin. Additional financial support was provided by the Natural Sciences and Engineering

Research Council of Canada. Part of this research was conducted while the first author was a graduate student at the University of Alberta and assistance from the Department of Civil Engineering is appreciated. Helpful suggestions from Dr. Derek Elsworth are appreciated.

## References

BANDIS, S.C. 1990. Mechanical properties of rock joints. Proceedings of the International Symposium on Rock Joints, 125-140.

BARTON, N. and BAKHTAR, K. 1983. Rock joint description and modeling for the hydro-thermo-mechanical design of nuclear waste repositories. CANMET, Mining Research Laboratories, Report TRE83-10, 258p.

CHAN, D.H. 1986. Analysis of Strain Softening Material. Ph.D. thesis, Dept. of Civil Engineering, University of Alberta, 345p.

CHAPPELL, B.A. 1990. Rock mass characterization for dam foundations. Journal of Geotechnical Engineering ASCE, **116**(GT4): 625-646.

EVERITT, R. 1986. Geology of the Room 209 area and its planned extension. Atomic Energy of Canada Limited, Report GSEB-86-168.

GOODMAN, R.E. and DUBOIS, J. 1972. Duplication of dilatancy in analysis of jointed rocks. Journal of the Soil Mechanics and Foundations Division ASCE, **98**(SM4): 399-422.

KAISER, P.K., CHAN, D.H., TANNANT, D.D., PELLI, F., and NEVILLE, C. 1987. Numerical Simulation of Room 209 Instrument Ring - Technical report to AECL, Pinawa, 200p.

KAISER, P.K., CHAN, D.H., TANNANT, D.D., and ZOU, D.H. 1989. Numerical Simulations of Room 209 Instrument Array - Technical report on data comparison and back analysis for AECL, Pinawa, 217p.

KATSUBE, T.J. and HUME, J.P. 1987. Geotechnical studies at Whiteshell Research Area (RA-3). CANMET report MRL 87-52.

KOOPMANS, R. and HUGHES, R.W. 1988. Determination of Excavation Disturbance in Room 209 Underground Research Laboratory. Ontario Hydro research division, 88-65-K.6.

_____ 1989a. The assessment of excavation disturbance surrounding underground openings in rock. Proceedings of a NEA Workshop on Excavation Responses in Geological Repositories for Radioactive Waste, Winnipeg, 283-294.

_____ 1989b. Reassessment of excavation disturbance in Room 209 - Underground Research Laboratory. Ontario Hydro research division, 89-308-K.27.

KOZAK, E.T. and DAVISON, C.C. 1986. Hydrogeological Conditions in a Vertical Fracture Intersecting Room 209 of the 240 m Level of the Underground Research Laboratory. Atomic Energy of Canada Limited report, Pinawa.

KUZYK, G.W., LANG, P.A. and BEL, G. 1986. Blast design and quality control at the second level of Atomic Energy of Canada's Underground Research Laboratory. Proceedings of the International Symposium on Large Rock Caverns, Helsinki, 1: 147-158.

LANG, P.A. 1989. Room 209 excavation response test in the Underground Research Laboratory. Proceedings of a NEA Workshop on Excavation Responses in Geological Repositories for Radioactive Waste, Winnipeg, 295-329.

LANG, P.A., EVERITT, R.A., KOZAK, E.T., DAVISON, C.C. 1986. Room 209 Instrument Array - Pre-excavation information for modellers. Atomic Energy of Canada Limited, Report AECL-9566-1.

LANG, P.A., KUZYK, G.W., BABULIC, P.J., BILINSKY, D.M., EVERITT, R.A., SPINNEY, M.H., KOZAK, E.T., and DAVISON, C.C. 1987. Room 209 Instrument Array: Measured Response to Excavation. Atomic Energy of Canada Limited TR-433, Whiteshell Nuclear Research Establishment.

MAKURAT, A. 1989. Coupled shear flow temperature tests (CSFT) on URL joint. Norwegian Geotechnical Institute, Report 876058.

MARTIN C.D., DAVISON, C.C. and KOZAK, E.T. 1990a. Characterizing normal stiffness and hydraulic conductivity of a major shear zone in granite. Proceedings of the International Symposium on Rock Joints, 549-556.

MARTIN C.D., READ R.S. and LANG P.A. 1990b. Seven years of in situ stress measurement at the URL - an overview. Proceedings of the 31th U.S. Symposium on Rock Mechanics, Golden, 15-26.

PYRAK-NOLTE, L.J., MYER, L.R., COOK, N.G.W. and WITHERSPOON, P.A. 1987. Hydraulic and mechanical properties of natural fractures in low permeability rock. Proceedings of 6th Congress of the International Society for Rock Mechanics, **1:** 225-231.

RAVEN, K.G. AND GALE, J.E. 1985. Water flow in a natural rock fracture as a function of stress and sample size. International Journal of Rock Mechanics and Mining Sciences & Geomechanics Abstracts, **22**(4): 251-261.

RUTQVIST, J., LJUNGGREN, C., STEPHANSSON, O., NOORISHAD, J. and TSANG, C.F. 1990. Theoretical and field investigations of fracture hydromechanical response under fluid injection. Proceedings of the International Symposium on Rock Joints, 557-564.

SUN, Z., GERRARD, C. and STEPHANSSON, O. 1985. Rock joint compliance tests for compression and shear loads. International Journal of Rock Mechanics and Mining Sciences & Geomechanics Abstracts, **22**(4): 197-213.

TANNANT, D.D. 1990. Hydraulic Response of a Fracture Zone to Excavation-Induced Shear. PhD. thesis, Dept. of Civil Engineering, University of Alberta, 189p.

TANNANT, D.D. and KAISER P.K. 1991. Interpretation of packer tests conducted during excavation through a fracture zone. Proceedings of 7th Congress of the International Society for Rock Mechanics, Aachen, (**1**): 627-630.

TANNANT, D.D. and KAISER P.K. 1992. A shear-dependent fracture zone transmissivity model. Submitted simultaneously to the Canadian Geotechnical Journal (Dec. 1991).

THOMPSON, P.M., KOZAK, E.T. and MARTIN, C.D. 1989. Rock displacement instrumentation and coupled hydraulic pressure/rock displacement instrumentation for use in a stiff crystalline rock. Proceedings of a NEA Workshop on Excavation Responses in Geological Repositories for Radioactive Waste, Winnipeg, 257-270.

THOMPSON, P.M. and LANG, P.A. 1987. Geomechanical instrumentation applications at the Canadian underground research laboratory. Proceedings of the 2nd International Symposium on Field Measurements in Geomechanics, Kobe, 963-983.

## List of Figures

## List of Tables

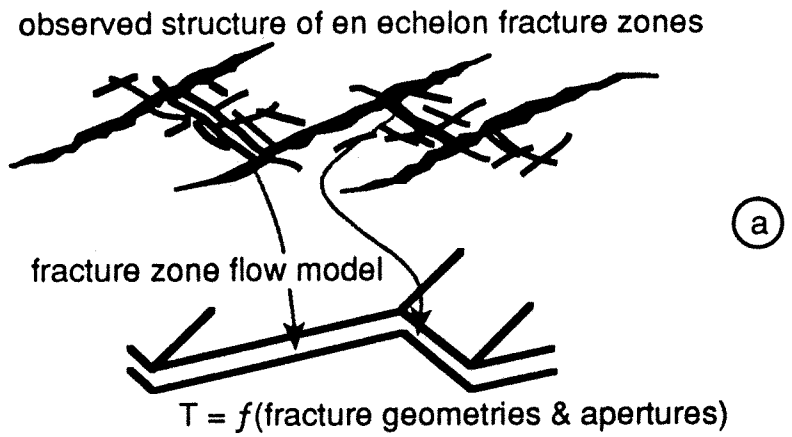
observed structure of en echelon fracture zones
a
fracture zone flow model
T = f(fracture geometries & apertures)

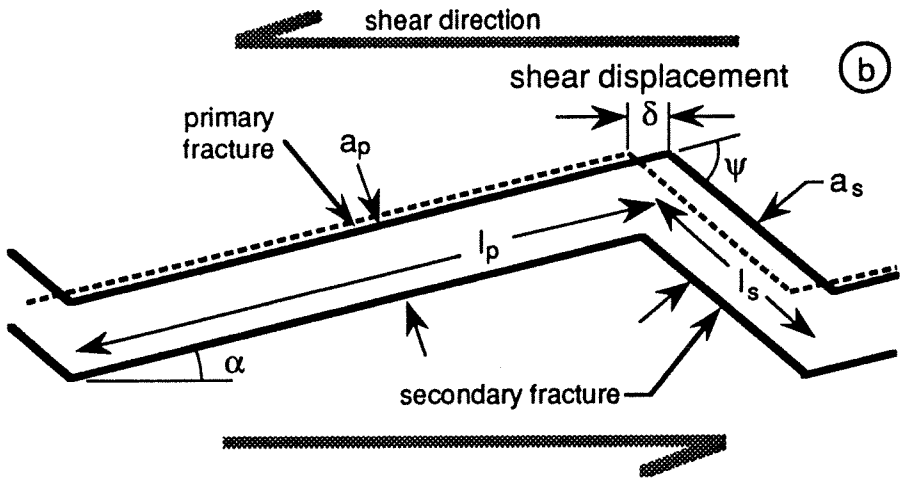
shear direction
shear displacement
b
primary fracture
$a_p$
$\delta$
$\psi$
$a_s$
$l_p$
$l_s$
$\alpha$
secondary fracture

Fig. 1

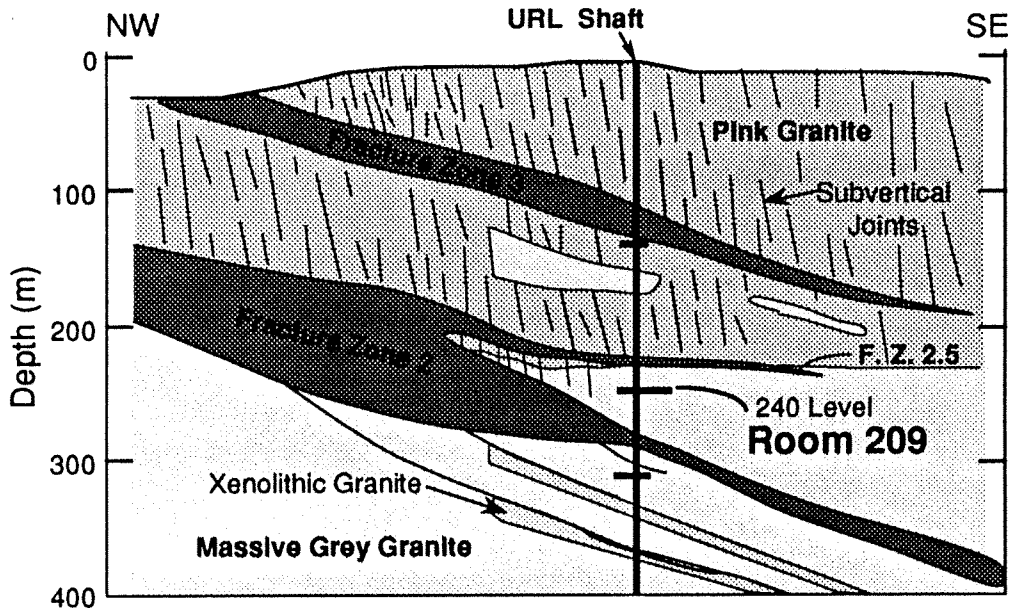
NW
URL Shaft
SE
0
100
200
300
400
Depth (m)
Fracture Zone 3
Pink Granite
Subvertical Joints
Fracture Zone 2
F. Z. 2.5
240 Level
Room 209
Xenolithic Granite
Massive Grey Granite

Fig. 2

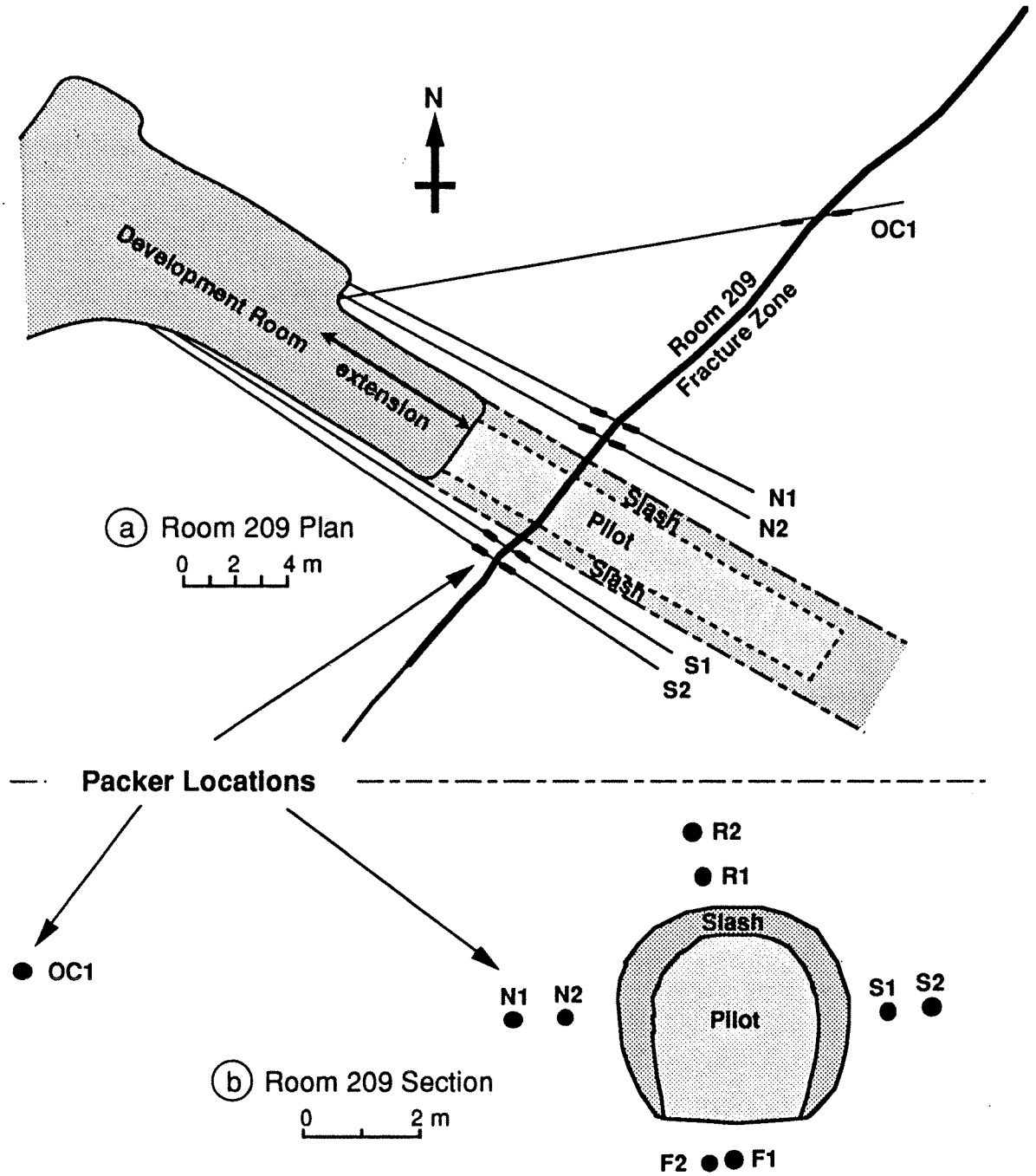
N
Development Room
extension
OC1
Room 209
Fracture Zone
N1
N2
Slash
Pilot
Slash
S1
S2
a Room 209 Plan
0 2 4 m
Packer Locations
R2
R1
OC1
N1 N2
Slash
Pilot
S1 S2
b Room 209 Section
0 2 m
F2 F1

Fig. 3

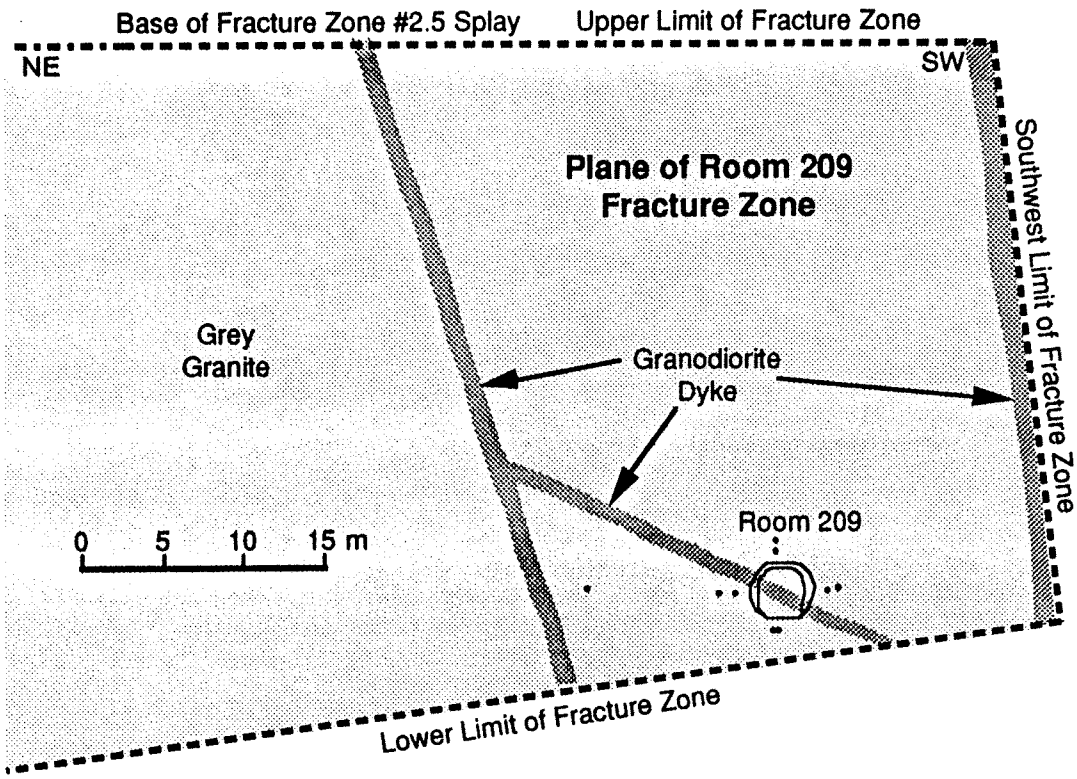
Base of Fracture Zone #2.5 Splay
Upper Limit of Fracture Zone
NE
SW
Plane of Room 209
Fracture Zone
Southwest Limit of Fracture Zone
Grey
Granite
Granodiorite
Dyke
Room 209
0 5 10 15 m
Lower Limit of Fracture Zone

Fig. 4

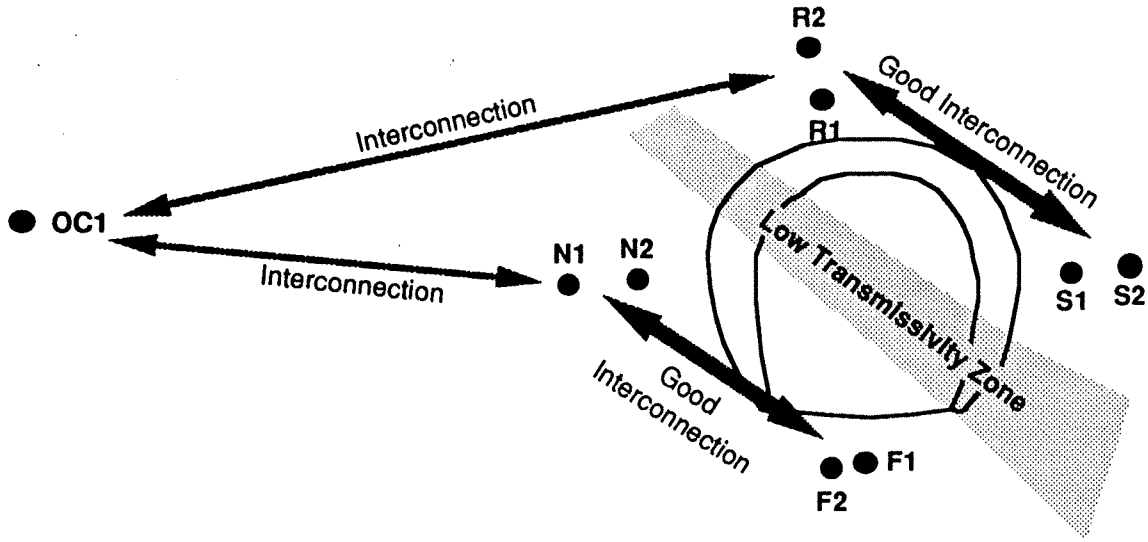
R2
R1
Interconnection
Good Interconnection
OC1
Interconnection
N1
N2
Low Transmissivity Zone
S1
S2
Good
Interconnection
F1
F2

Fig. 5

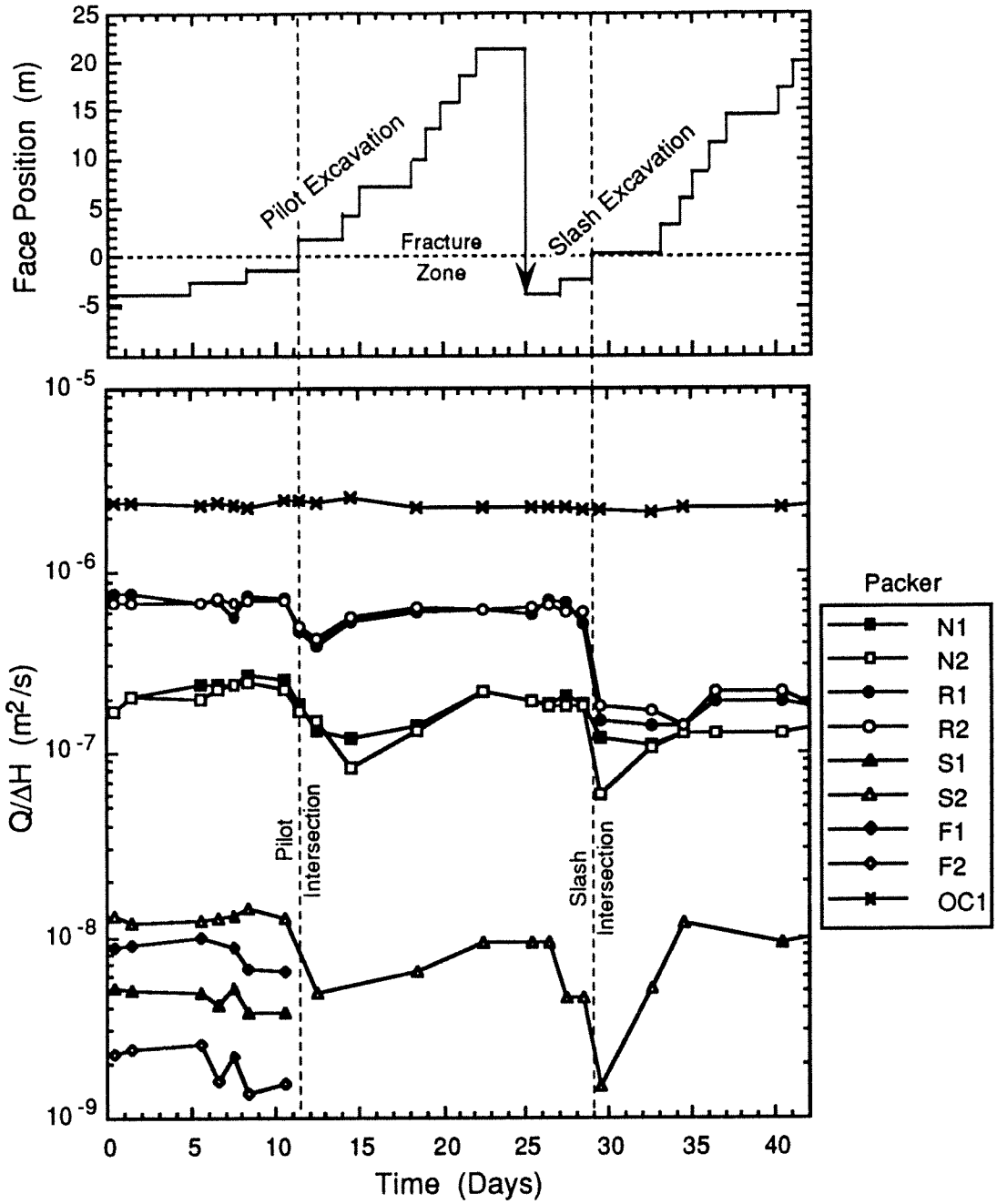
Face Position (m)
25
20
15
10
5
0
-5
Pilot Excavation
Fracture Zone
Slash Excavation
Q/ΔH (m²/s)
10⁻⁵
10⁻⁶
10⁻⁷
10⁻⁸
10⁻⁹
Pilot Intersection
Slash Intersection
0
5
10
15
20
25
30
35
40
Time (Days)
Packer
N1
N2
R1
R2
S1
S2
F1
F2
OC1

Fig. 6

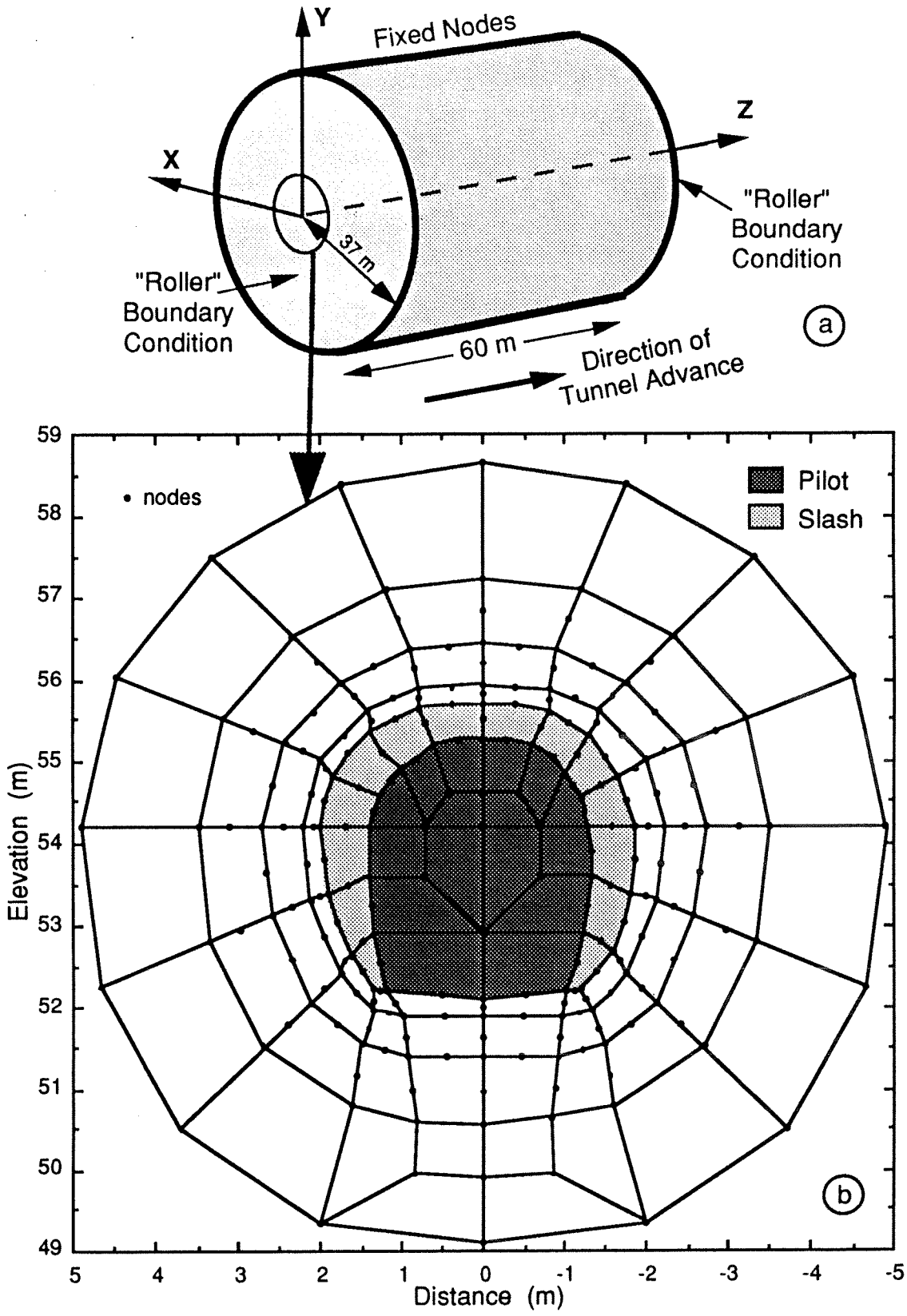
Y
Fixed Nodes
Z
X
"Roller"
Boundary
Condition
37 m
"Roller"
Boundary
Condition
a
60 m
Direction of
Tunnel Advance
• nodes
Pilot
Slash
Elevation (m)
59
58
57
56
55
54
53
52
51
50
49
5
4
3
2
1
0
-1
-2
-3
-4
-5
Distance (m)
b

Fig. 7

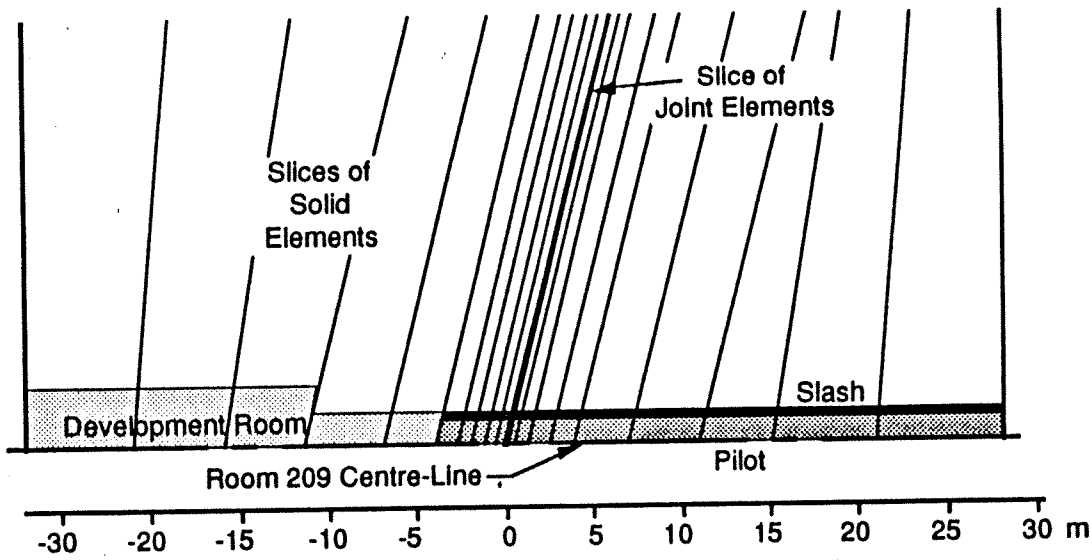
Slice of
Joint Elements
Slices of
Solid
Elements
Slash
Development Room
Pilot
Room 209 Centre-Line
-30
-20
-15
-10
-5
0
5
10
15
20
25
30 m

Fig. 8

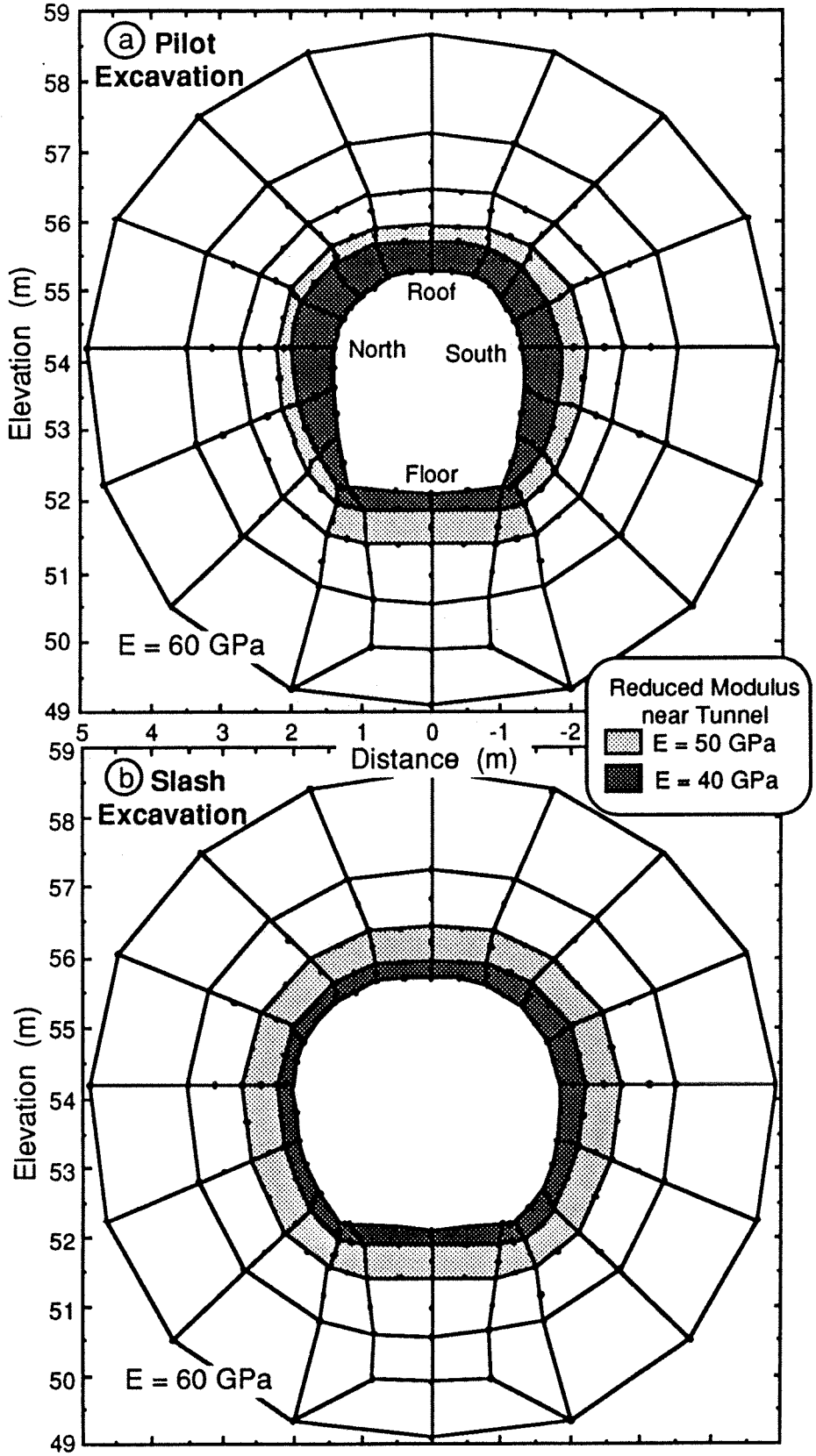
a Pilot Excavation
Roof
North
South
Floor
E = 60 GPa
Elevation (m)
59
58
57
56
55
54
53
52
51
50
49
5
4
3
2
1
0
-1
-2
Distance (m)
Reduced Modulus near Tunnel
E = 50 GPa
E = 40 GPa
b Slash Excavation
E = 60 GPa
Elevation (m)

Fig. 9

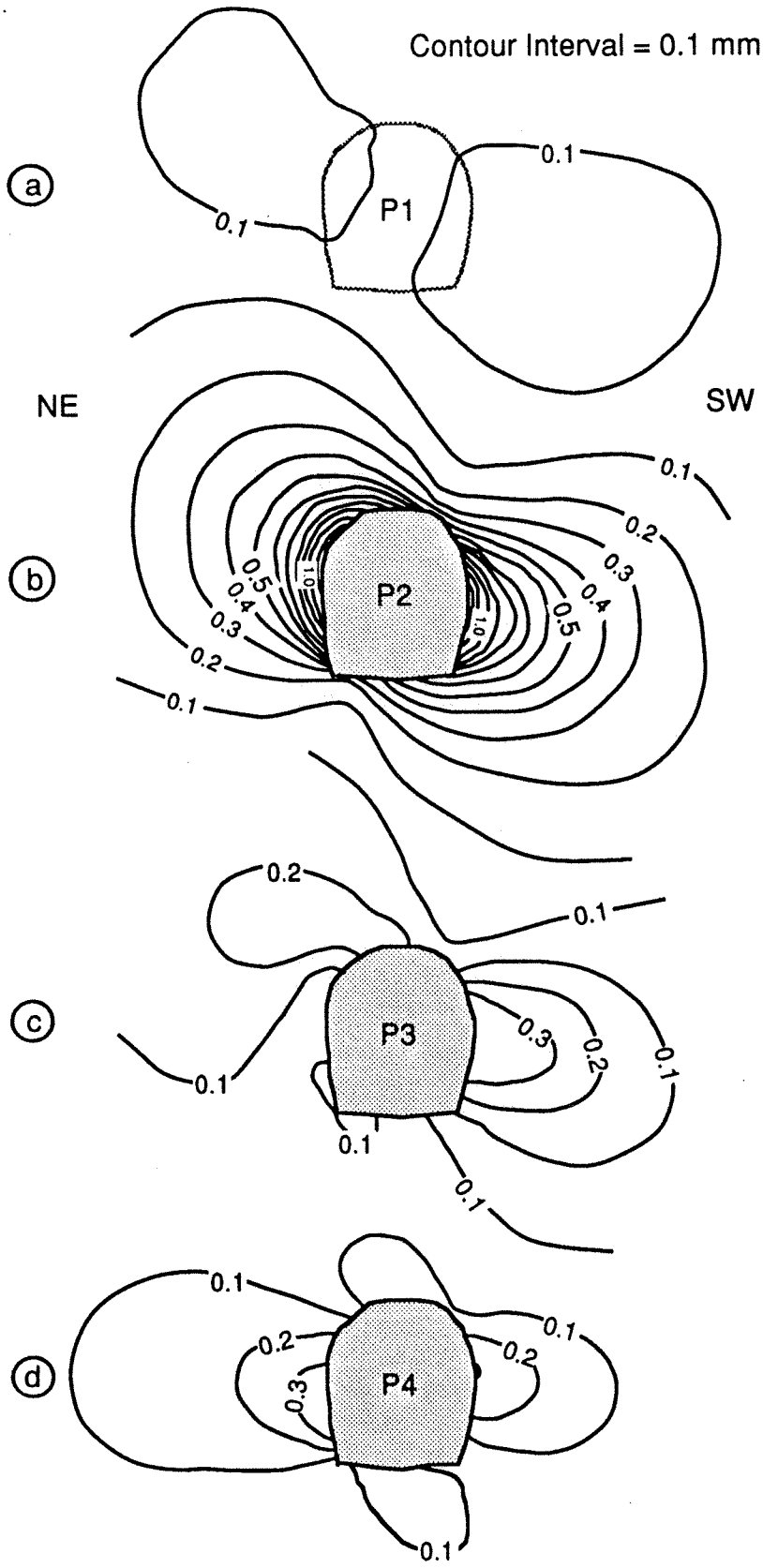
Contour Interval = 0.1 mm
a
P1
0.1
0.1
NE
SW
b
P2
0.1
0.2
0.3
0.4
0.5
0.5
0.4
0.3
0.2
0.1
c
P3
0.2
0.1
0.3
0.2
0.1
0.1
0.1
d
P4
0.1
0.2
0.3
0.1
0.2
0.1

Fig. 10

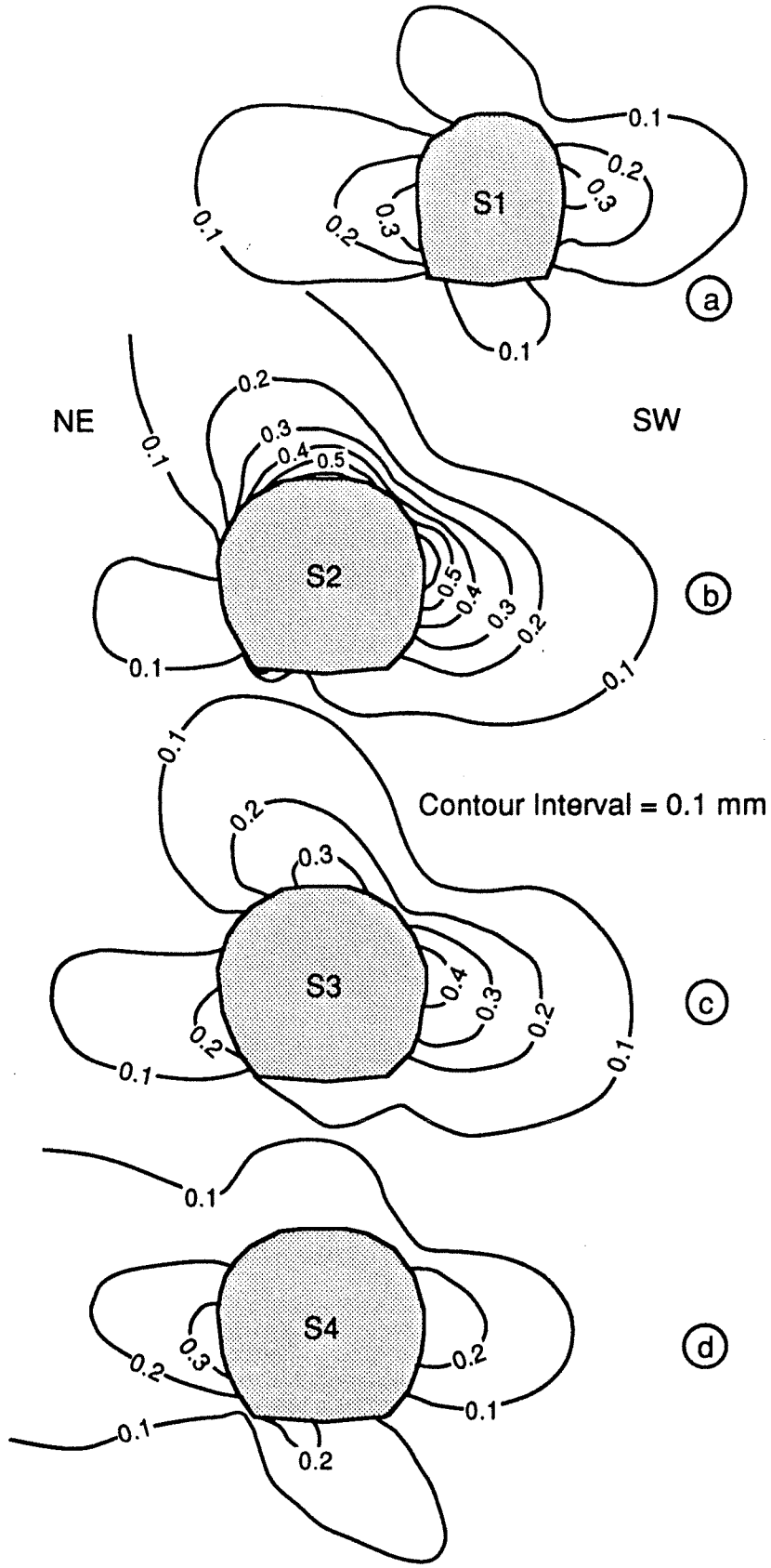
S1
0.1
0.2
0.3
0.1
0.2
0.3
0.1
a
NE
SW
S2
0.2
0.3
0.4
0.5
0.1
0.5
0.4
0.3
0.2
0.1
0.1
b
Contour Interval = 0.1 mm
S3
0.1
0.2
0.3
0.4
0.3
0.2
0.2
0.1
0.1
c
S4
0.1
0.2
0.3
0.2
0.2
0.1
0.1
0.2
d

Fig. 11

No Flow
B
C
Room 209 Tunnel
0 5 10 15 20 m
Constant Head @ 74.6 m
No Flow
A
Hydrostatic Increase in Head to 139.3 m @ D
D

Fig. 12

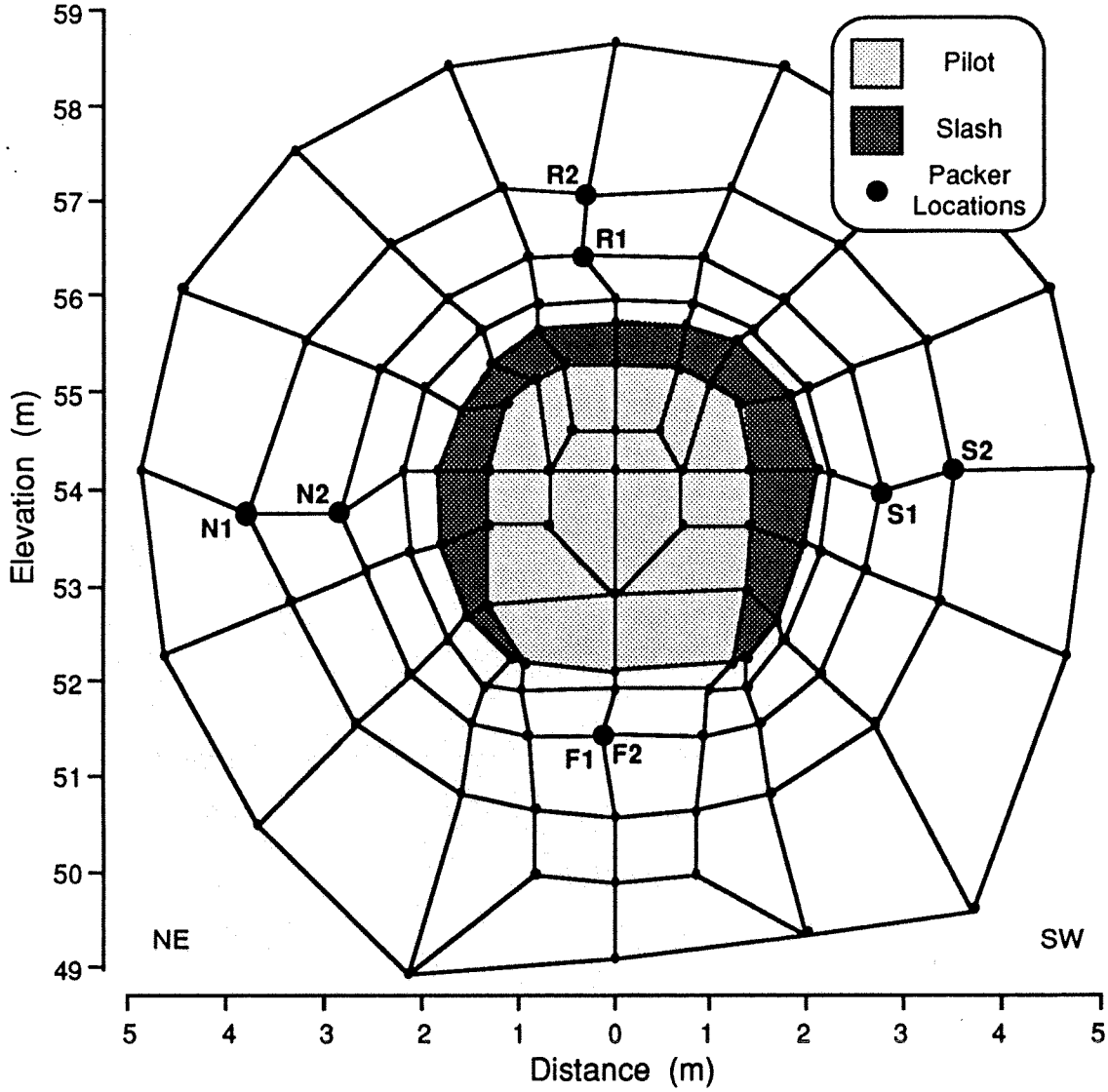
Pilot
Slash
Packer Locations
R2
R1
S2
S1
N2
N1
F1
F2
NE
SW
Elevation (m)
59
58
57
56
55
54
53
52
51
50
49
5
4
3
2
1
0
1
2
3
4
5
Distance (m)

Fig. 13

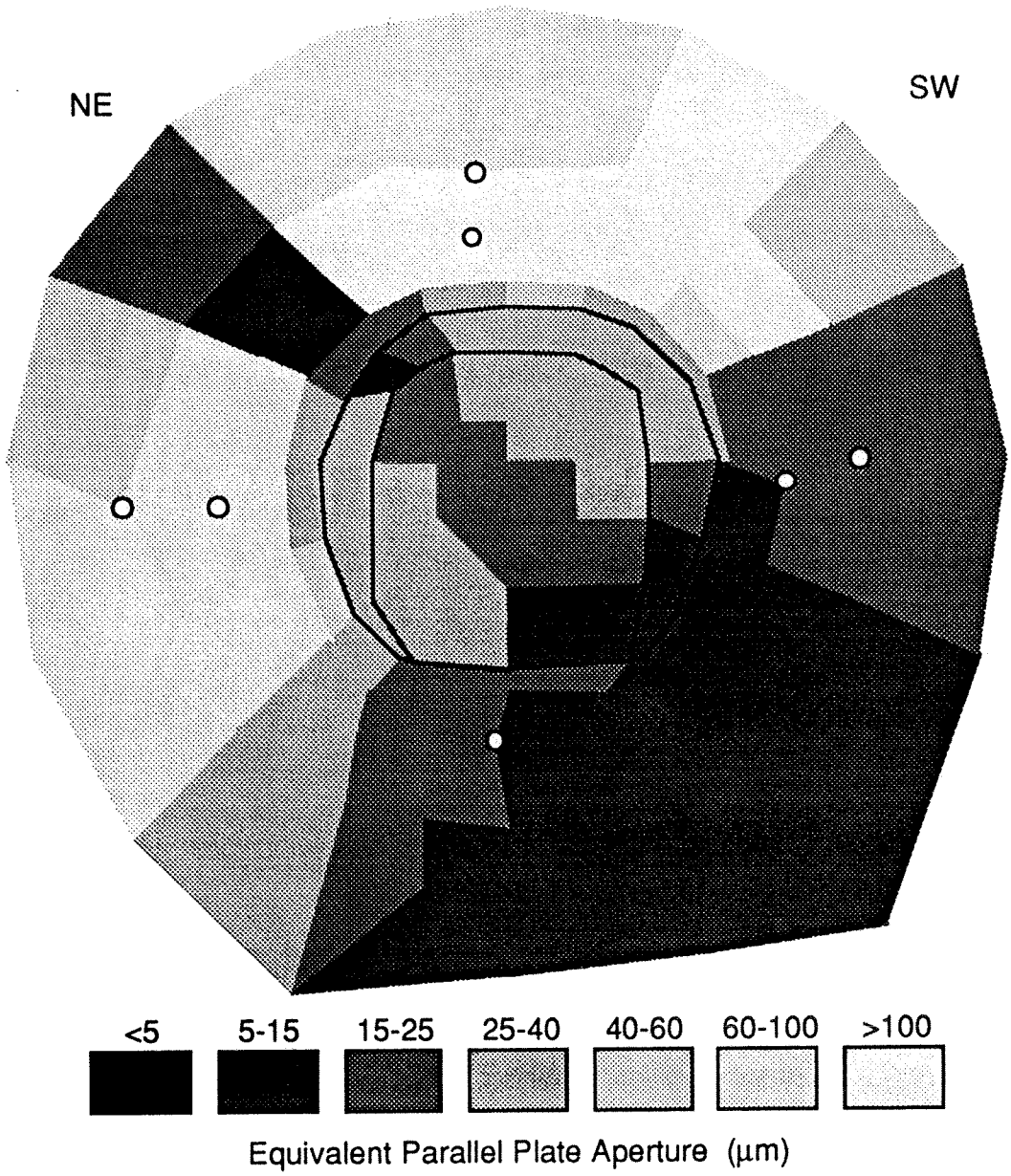
NE
SW
<5
5-15
15-25
25-40
40-60
60-100
>100
Equivalent Parallel Plate Aperture (μm)

Fig. 14

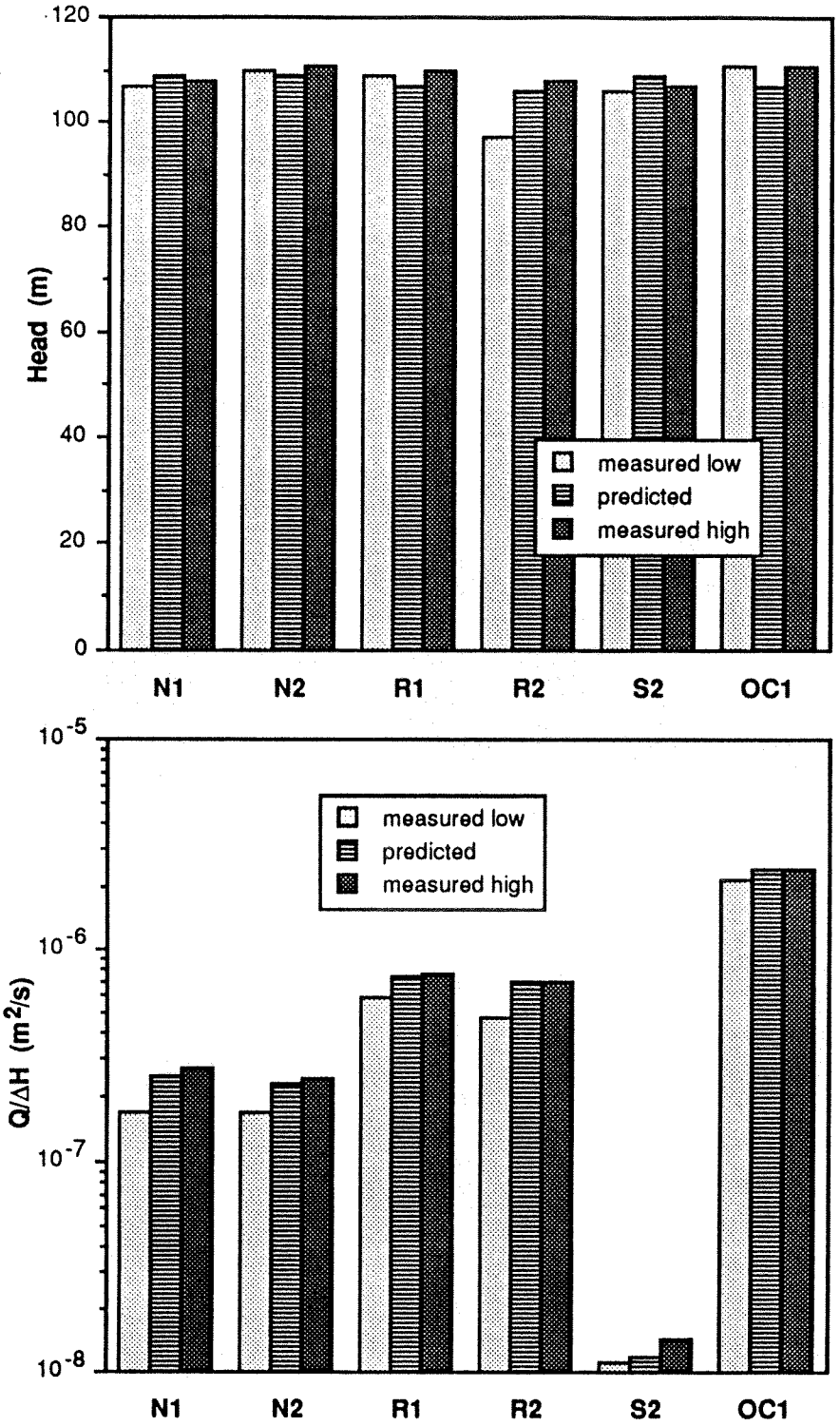
120
100
80
60
40
20
0
Head (m)
measured low
predicted
measured high
N1
N2
R1
R2
S2
OC1
$10^{-5}$
$10^{-6}$
$10^{-7}$
$10^{-8}$
$Q/\Delta H$ ($m^2/s$)
measured low
predicted
measured high
N1
N2
R1
R2
S2
OC1

Fig. 15

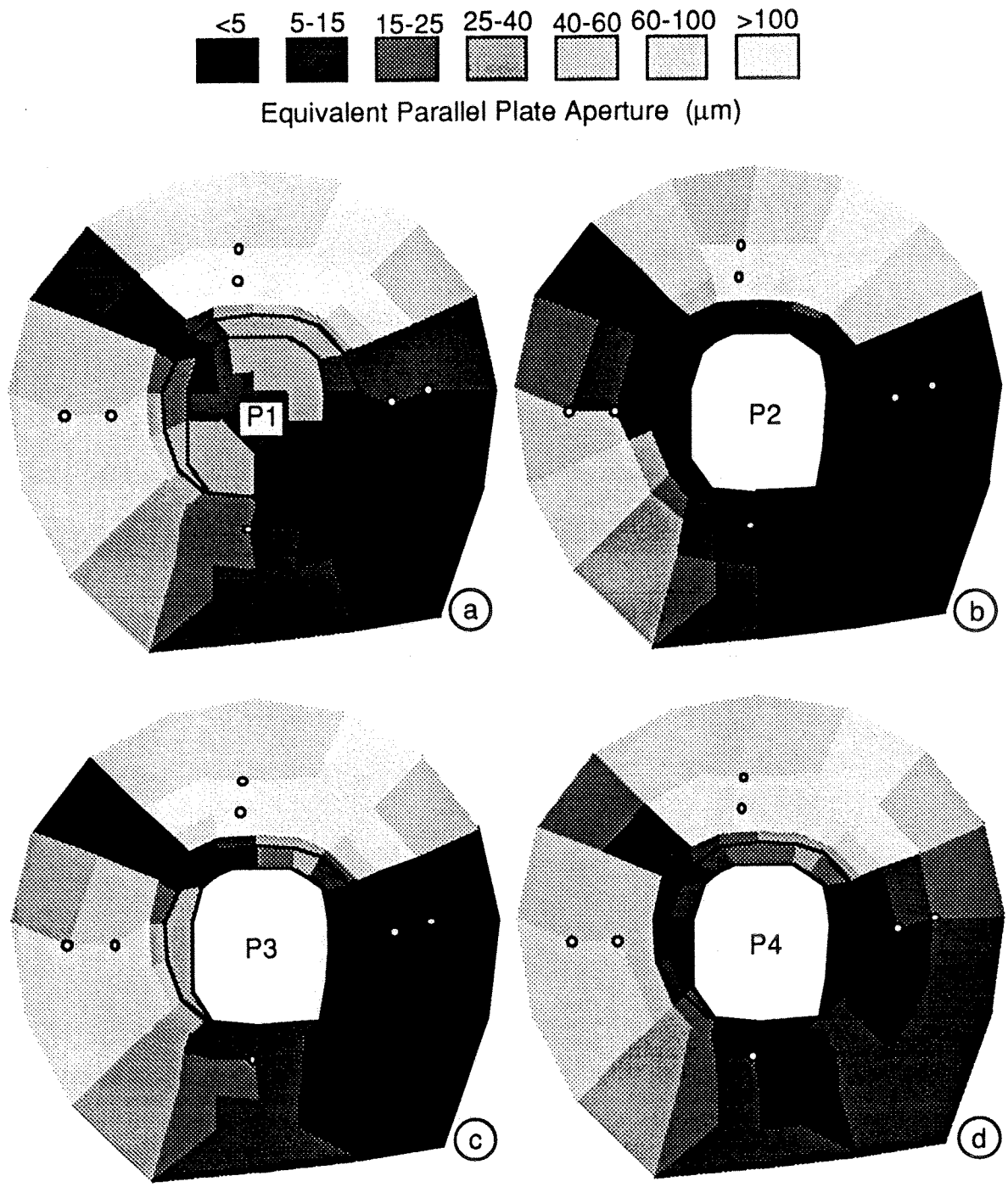
<5
5-15
15-25
25-40
40-60
60-100
>100
Equivalent Parallel Plate Aperture (μm)
P1
P2
P3
P4
a
b
c
d

Fig. 16

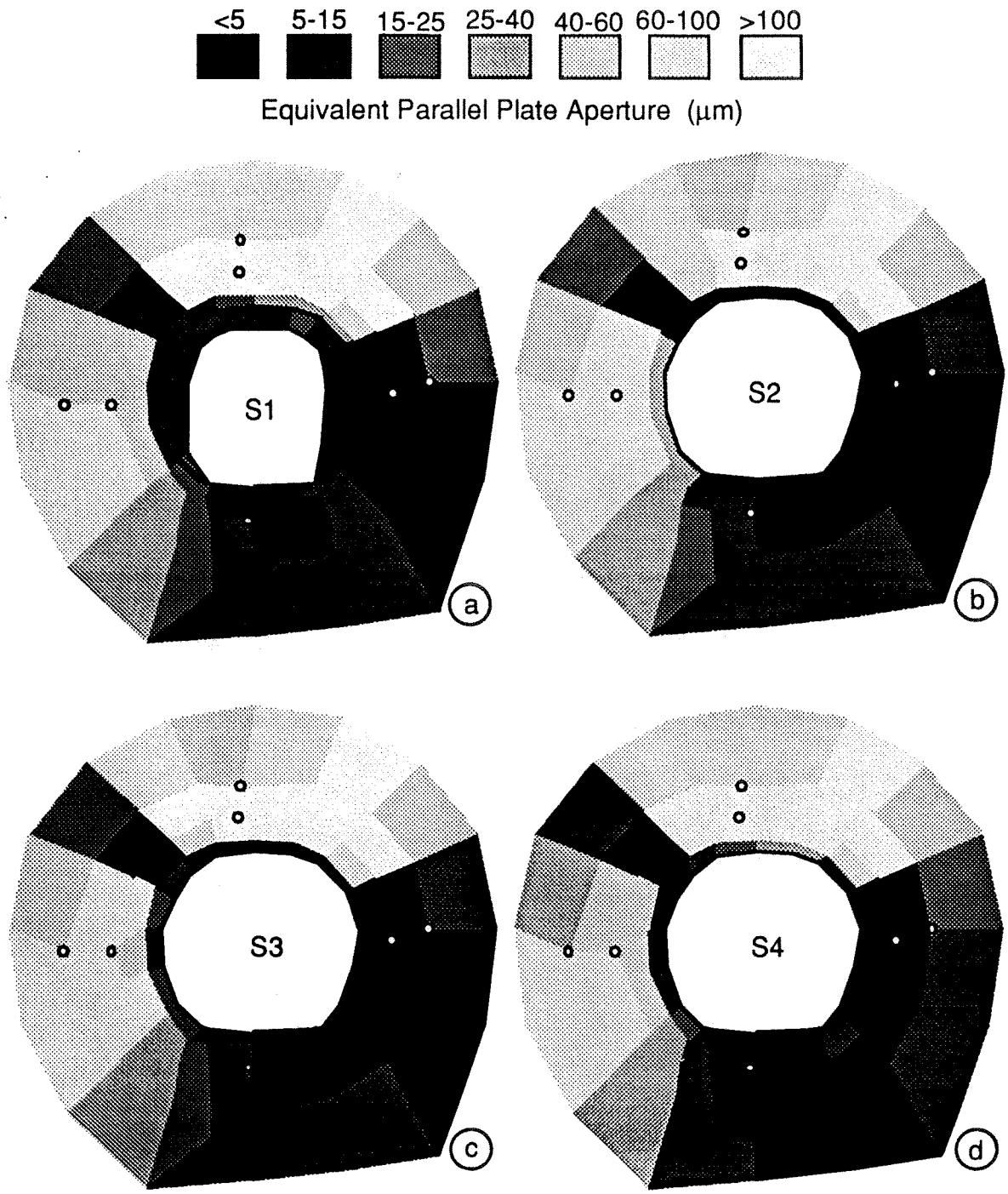
<5
5-15
15-25
25-40
40-60
60-100
>100
Equivalent Parallel Plate Aperture (μm)
S1
a
S2
b
S3
c
S4
d

Fig. 17

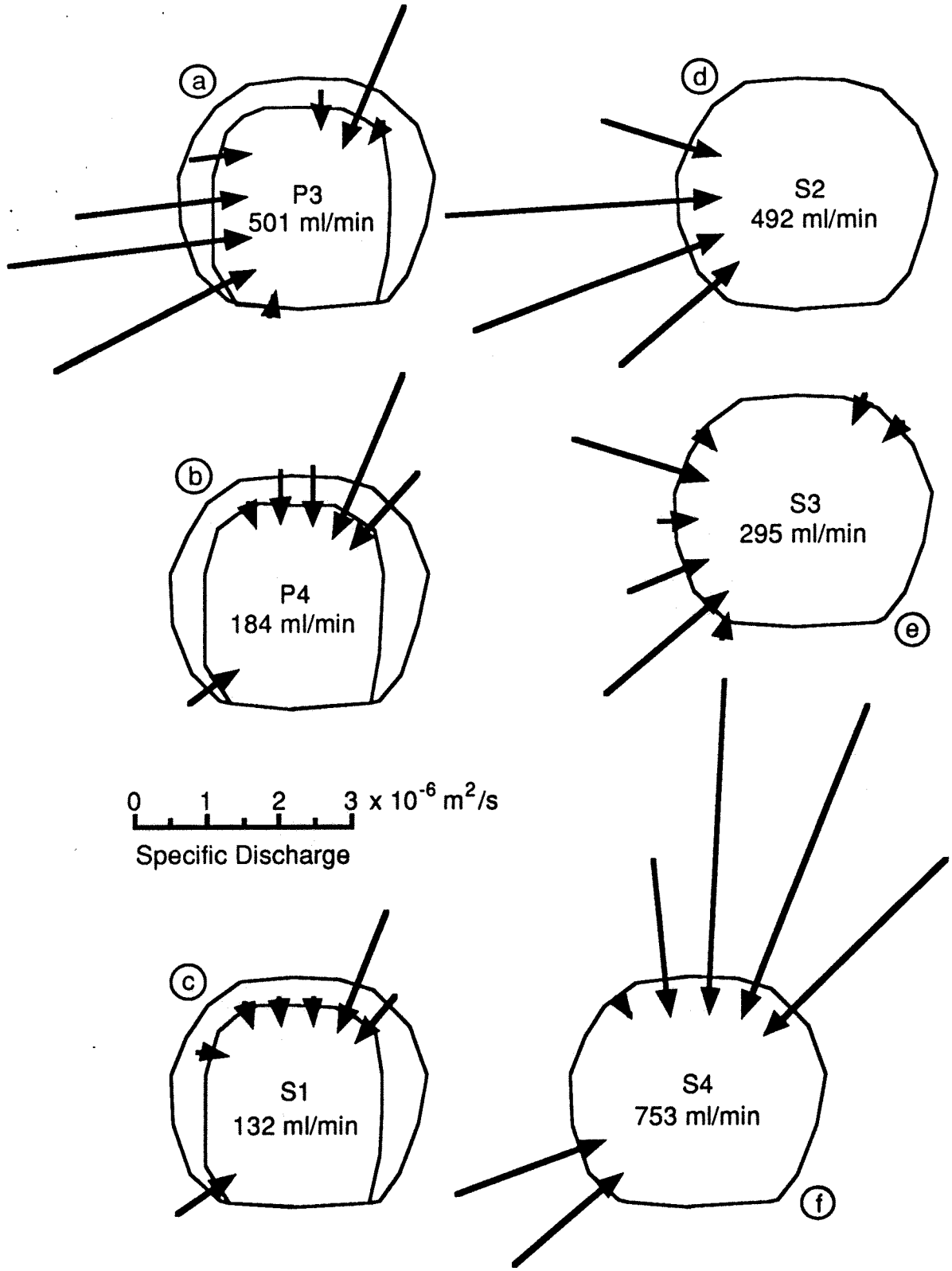
a
P3
501 ml/min
d
S2
492 ml/min
b
P4
184 ml/min
S3
295 ml/min
e
0 1 2 3 x 10-6 m2/s
Specific Discharge
c
S1
132 ml/min
S4
753 ml/min
f

Fig. 18

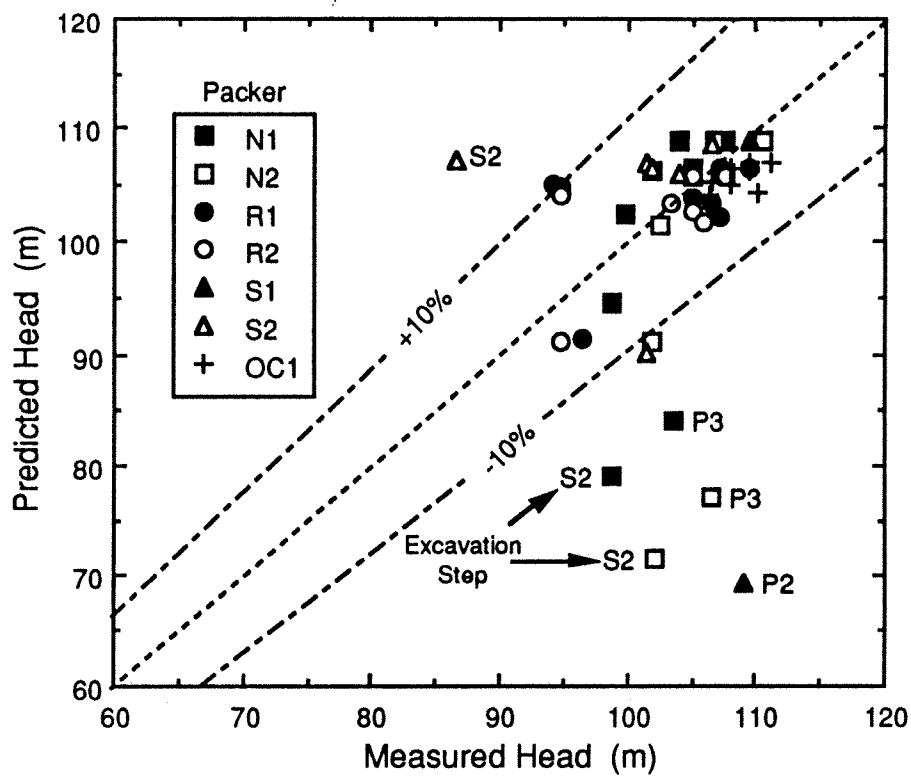
Packer
N1
N2
R1
R2
S1
S2
OC1
+10%
-10%
S2
P3
S2
P3
Excavation
Step
S2
P2
Predicted Head (m)
Measured Head (m)
120
110
100
90
80
70
60
60
70
80
90
100
110
120

Fig. 19

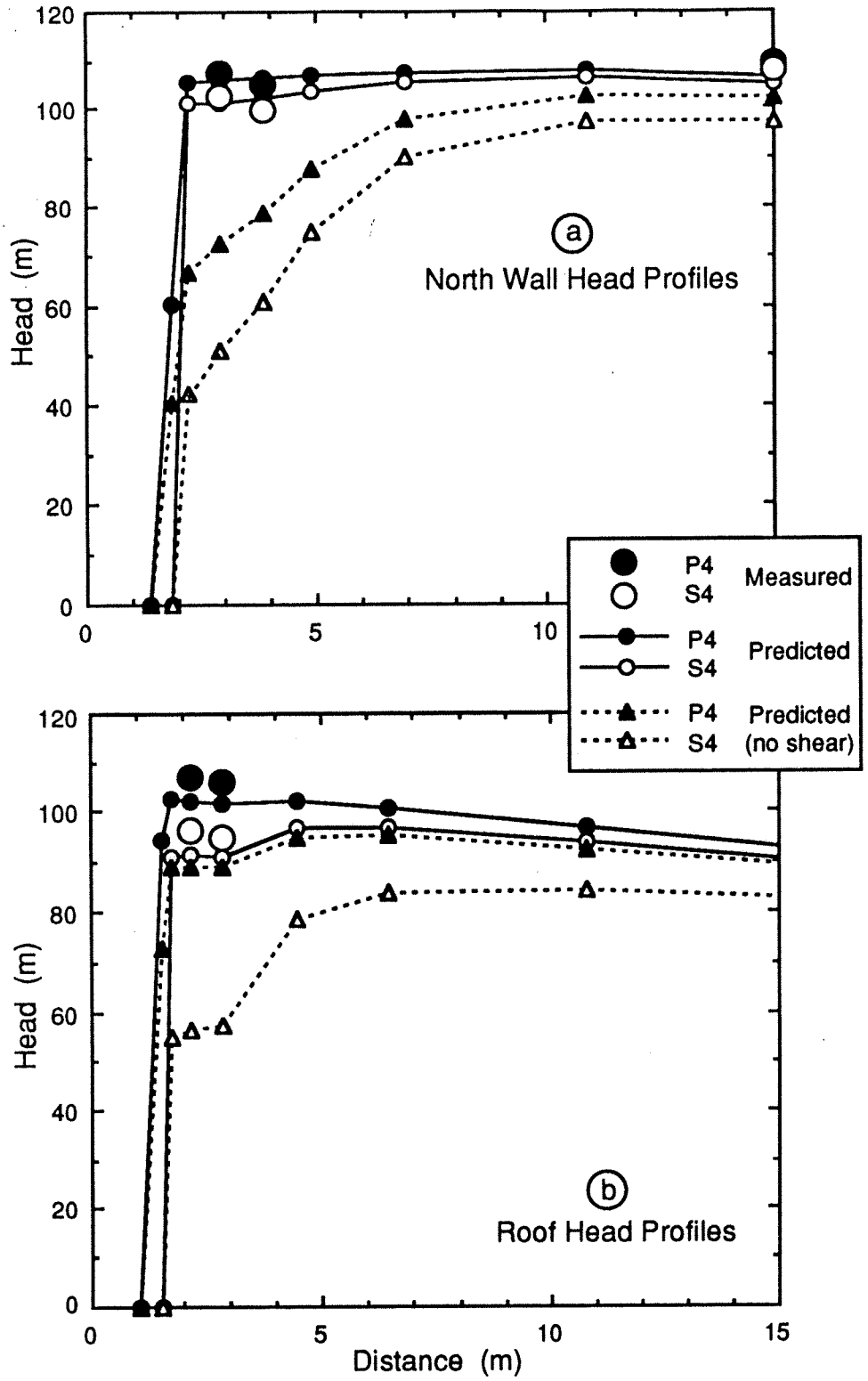
120
100
80
60
40
20
0
Head (m)
0
5
10
15
Distance (m)
a
North Wall Head Profiles
b
Roof Head Profiles
P4
S4
Measured
P4
S4
Predicted
P4
S4
Predicted
(no shear)

Fig. 20

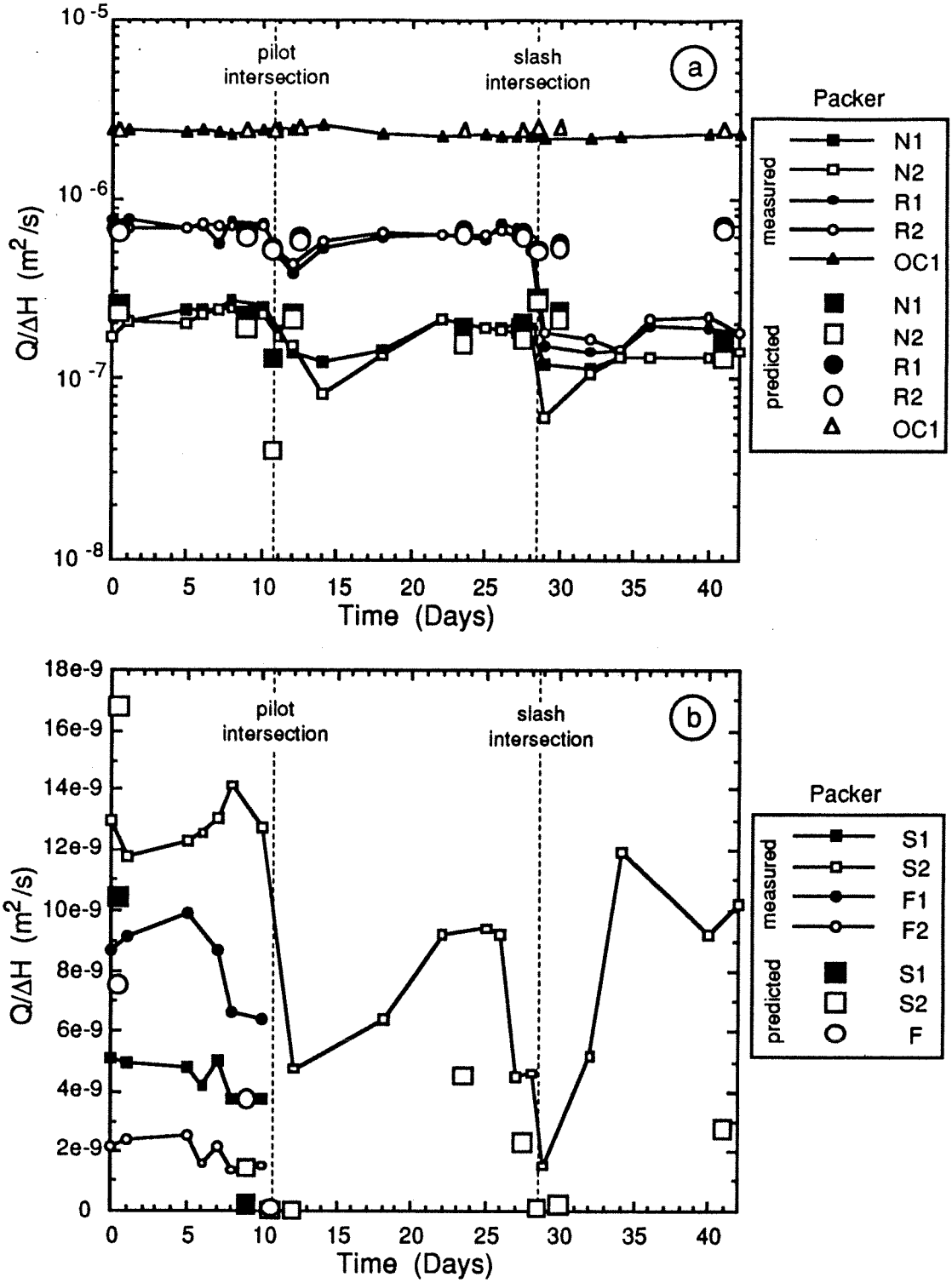
a
pilot intersection
slash intersection
Q/ΔH (m²/s)
Time (Days)
Packer
measured
N1
N2
R1
R2
OC1
predicted
N1
N2
R1
R2
OC1
b
pilot intersection
slash intersection
Q/ΔH (m²/s)
Time (Days)
Packer
measured
S1
S2
F1
F2
predicted
S1
S2
F

Fig. 21

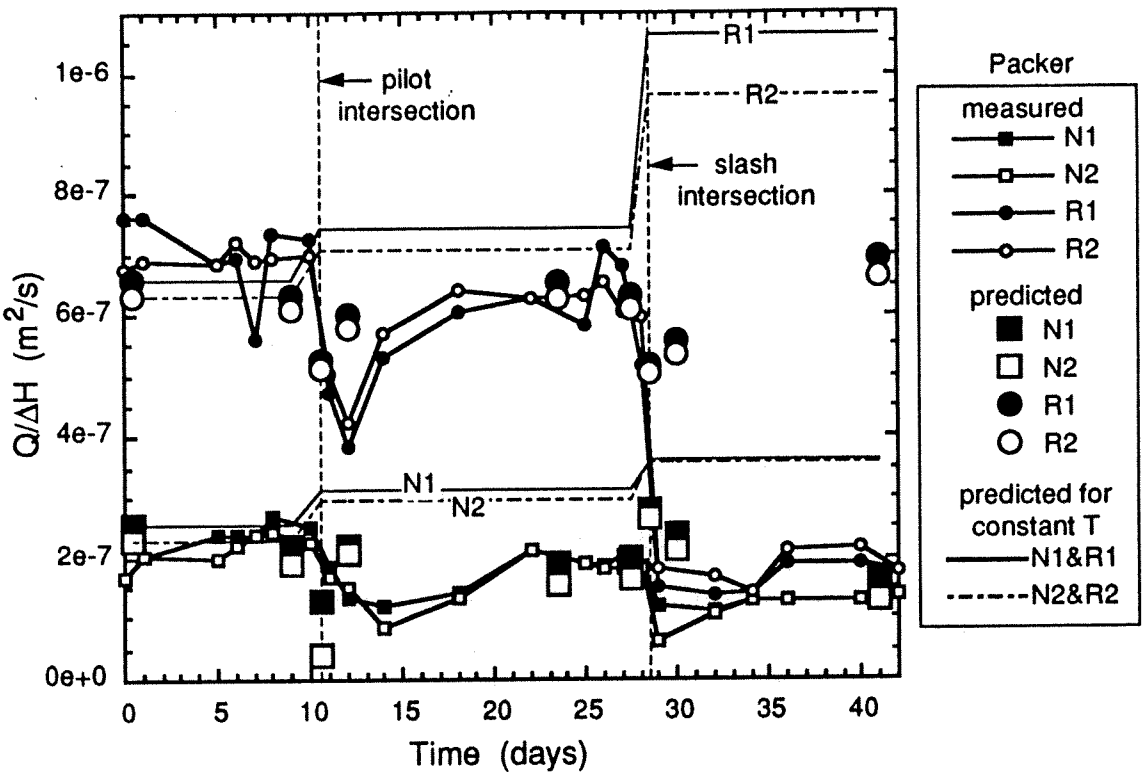
R1
R2
pilot intersection
slash intersection
N1
N2
1e-6
8e-7
6e-7
4e-7
2e-7
0e+0
Q/ΔH (m²/s)
0
5
10
15
20
25
30
35
40
Time (days)
Packer
measured
N1
N2
R1
R2
predicted
N1
N2
R1
R2
predicted for constant T
N1&R1
N2&R2

Fig. 22